



THE UNIVERSITY *of* EDINBURGH

Edinburgh Research Explorer

The interplay of magmatism and tectonics: An example based on the satellite scoria cones at Llaima volcano, Chile.

Citation for published version:

Schonwalder, D, Cortes, JA & Calder, E 2018, 'The interplay of magmatism and tectonics: An example based on the satellite scoria cones at Llaima volcano, Chile.', *Journal of Volcanology and Geothermal Research*, vol. 367, pp. 31-45. <https://doi.org/10.1016/j.jvolgeores.2018.10.020>

Digital Object Identifier (DOI):

[10.1016/j.jvolgeores.2018.10.020](https://doi.org/10.1016/j.jvolgeores.2018.10.020)

Link:

[Link to publication record in Edinburgh Research Explorer](#)

Document Version:

Peer reviewed version

Published In:

Journal of Volcanology and Geothermal Research

General rights

Copyright for the publications made accessible via the Edinburgh Research Explorer is retained by the author(s) and / or other copyright owners and it is a condition of accessing these publications that users recognise and abide by the legal requirements associated with these rights.

Take down policy

The University of Edinburgh has made every reasonable effort to ensure that Edinburgh Research Explorer content complies with UK legislation. If you believe that the public display of this file breaches copyright please contact openaccess@ed.ac.uk providing details, and we will remove access to the work immediately and investigate your claim.



Accepted Manuscript

The interplay of magmatism and tectonics: An example based on the satellite scoria cones at Llaima volcano, Chile

Dayana Schonwalder-Angel, Joaquín A. Cortés, Eliza S. Calder



PII: S0377-0273(18)30213-0

DOI: <https://doi.org/10.1016/j.jvolgeores.2018.10.020>

Reference: VOLGEO 6475

To appear in: *Journal of Volcanology and Geothermal Research*

Received date: 28 May 2018

Revised date: 19 October 2018

Accepted date: 22 October 2018

Please cite this article as: Dayana Schonwalder-Angel, Joaquín A. Cortés, Eliza S. Calder , The interplay of magmatism and tectonics: An example based on the satellite scoria cones at Llaima volcano, Chile. Volgeo (2018), <https://doi.org/10.1016/j.jvolgeores.2018.10.020>

This is a PDF file of an unedited manuscript that has been accepted for publication. As a service to our customers we are providing this early version of the manuscript. The manuscript will undergo copyediting, typesetting, and review of the resulting proof before it is published in its final form. Please note that during the production process errors may be discovered which could affect the content, and all legal disclaimers that apply to the journal pertain.

**The interplay of magmatism and tectonics: An example based on the
satellite scoria cones at Llaima volcano, Chile**

Dayana Schonwalder-Angel^{1*}, Joaquín A. Cortés^{2,3}, and Eliza S. Calder³

¹ Earth Observatory of Singapore, Nanyang Technological University, 50 Nanyang Ave.,
639798, Singapore

² Department of Geography, Edge Hill University, Ormskirk, Lancashire, L39 4QP, UK

³ School of Geosciences, University of Edinburgh, Grant Institute. The King's Buildings, West
Mains Road. Edinburgh EH9 3JW, UK

To be re-submitted to JVGR. September 2018

Corresponding author: Dayana Schonwalder-Angel (e-mail: angel.d@ntu.edu.sg)

Abstract

We present a geochemical and mineralogical study of the satellite scoria cones at Llaima volcano, Chile, providing insights on magmatic processes and how these are affected by the local and regional tectonics. At Llaima, we identify two different and distinctive groups of satellite scoria cones with a common magmatic source but different petrological evolutions. Cones from group 1 (the “glomeroporphyritic group”), predominantly occur in the NE flank of the volcano, are characterized by basaltic to basaltic andesitic compositions (51-55 wt. % SiO₂) and have glomeroporphyritic textures. We have interpreted these cones as the product of magma replenishment, followed by an unimpeded propagation of their feeder dikes controlled mainly by the regional stress. As a result, dikes are emplaced parallel to the regional σ_1 , and perpendicular to the axis of local crustal extension. Cones from the group 2 (the “pilotalitic group”), appear at the NE, NW and SW flanks of the volcano, they have more evolved compositions (55-60 wt. % SiO₂) and textures lacking glomerocrysts. Their location and morphometric parameters suggest that their feeder dike emplacement is mainly controlled by the stress exerted by the load of the volcanic edifice, where the compressional stress hinders magma ascent, allowing fractionation and volatile overpressure buildup. The characteristic texture of these cones is interpreted as fractionation, followed by a single crystallization event upon eruption. The lack of scoria cones at the SE flank is attributed to the local horizontal compressional stress caused by the local tectonic deformation associated to the Liquiñe-Ofqui Fault Zone.

Key Words: Llaima volcano, magma recharge, volcanic plumbing, dike emplacement, regional stress.

1. Introduction

Composite volcanoes often have complex plumbing systems, composed of short-lived magma bodies and regions of crystal-rich mush (Sparks and Cashman, 2017). These plumbing systems are geometrically-controlled by the interplay of magmatism with the local and the regional tectonics (Cembrano and Lara, 2009), although little is known on the extent and mechanisms of such control. In this work we explore this interaction, focusing on monogenetic scoria cones and fissures occurring around the main edifice of a composite volcano.

The spatial distribution of scoria cones and their chemical, textural and mineralogical variations are the surface expression of magma injection through the dikes that constitute the volcano plumbing system (Nakamura, 1977; Tibaldi, 2015). Their spatial location is essentially controlled by the state of stress at shallow levels of the crust (Nakamura, 1977); which in turn is a consequence of the influence of a magma reservoir, the loading of the volcanic edifice and mechanical differences in its lithology (Pinel and Jaupart, 2000; Poland et al., 2004). These influences are negligible, both horizontally and at depth, away from the reservoir and the footprint of the volcanic edifice, rendering the local stress field similar to the regional stress (Gudmundsson, 2006; Roman and Jaupart, 2014).

Magma reservoirs are located at shallow and brittle levels of the crust and the models of these reservoirs, such as oblate-ellipsoid (Gudmundsson, 2012), represent an abstraction of the crystal-rich mush and pockets of melt zones (Sparks and Cashman, 2017). Intrusions, such as dikes, sills, and cone-sheets that propagate from this area, will be influenced by the local stress field developed around it (Takada, 1994; Gudmundsson, 2006). Dikes initiate at the upper margins of the reservoir, and are favored by an increase of the concentration of the maximum tensile stress, caused by the reservoir's vicinity to the surface and the local stress field

imposed by the load of the volcanic edifice (Muller et al., 2001). Beneath the volcanic edifice, the shallow compressive stress impedes the ascent of dense primitive magmas favoring horizontal propagation away from the edifice, with dikes resuming vertical propagation at distances equal to the edifice radius. However, if magma buoyancy overcome the pressure barrier imposed by the edifice, vertical propagation in the focal area is possible (Roman and Jaupart, 2014). Sill emplacement is controlled by the mechanical anisotropy of the country rock that locally reorganizes the state of stress arresting or deviating the propagating dike (Valentine and Krogh, 2006; Geshi et al., 2012). Cone-sheets are conical and concentrically organized intrusions generated at the upper part of the reservoir, and are formed due to overpressure at the magma reservoir (Anderson, 1936; Mathieu et al., 2015). In general, dike emplacement depends on the state of the stress in the crust modified by the physical discontinuity posed by the presence of a magma reservoir and the volcanic edifice load, where vertical dikes occur when σ_3 is horizontal and their orientations follow either σ_1 or σ_2 (Valentine and Krogh, 2006).

Additionally, the chemistry, textures and mineralogy found in the products erupted by the scoria cones also depends on this underlying geometry as well as processes occurring at the reservoir and during dike propagation (Strong and Wolff, 2003). If it is established that dikes are fed by a common magmatic source, then differences in textures, whole-rock and mineral compositions, are due to later processes occurring in the sub-volcanic plumbing system (Mollo et al., 2011). A reflection of the complexity of volcanic plumbing can be assessed by characteristics such as mafic compositions and ferromagnesian phenocrysts-rich textures attributed to influx of new magma into the reservoir, or intermediate compositions and phenocryst-poor magmas attributed to crystallization and fractionation (Johnson et al., 2008; Almeev et al., 2013). While crystallization, fractionation and degassing are likely to occur at

the reservoir, they can also occur at different regions of the plumbing (i.e. the propagating dike) due to decompression, where magma ascent rate governs how such processes occur (Cashman and Blundy, 2000; Hammer and Rutherford, 2002). For example, when magma rises rapidly at a constant rate, crystal nucleation is the main process. If the rise of magma is slow at a constant rate, crystal growth dominates. If magma rises rapidly but not at a constant rate, vesiculation dominates and crystallization might be inhibited (Rutherford, 2008; Mollo and Hammer, 2017).

Here we examine that petrological and textural characteristics of scoria cone products combined with the study of their spatial distribution and morphology, to fully characterize volcanic plumbing based on these models. We use the highly-active Llaima volcanic system (Petit-Breuilh, 2006; Bouvet De Maisonneuve et al., 2013; Ruth et al., 2016), as a natural laboratory to test our assumptions. We show that textural, compositional and mineralogical differences between the scoria cones at Llaima, *reflect not only processes occurring at the magma reservoir but also during dike emplacement and eruption*. We also show that *petrological characteristics reflect the relationship between dike emplacement and the local and regional state of stresses*.

2. Geological Background

Llaima volcano ($38^{\circ}41'S$, $71^{\circ}43'W$; Fig. 1a) is located in the Southern South Volcanic Zone (SSVZ) of the Andes (Stern et al., 2007), where subduction is characterized by the oblique convergence ($22-30^{\circ}$ NE) of the Nazca Plate below the South American Plate (Pardo-Casas and Molnar, 1987; Cembrano and Lara, 2009). At the SSVZ, the Liquiñe-Ofqui Fault Zone (LOFZ) accommodates the tectonic deformation caused by oblique convergence (Fig. 1b), generating transpression and an arc-orthogonal extension setting that seems to be the main

control for the magma migration in the region (Cembrano et al., 1996). The LOFZ is a 1200 km long strike-slip intra-arc fault. It has been interpreted as a crustal-scale duplex structure with neotectonic dextral transpressional kinematics, active since the Eocene (48 Ma) and only interrupted during the Miocene (20 to 26 Ma) by a period of under-thrusting deformation associated with the orthogonal convergence of the Nazca plate under the South American plate (Pardo-Casas and Molnar, 1987; Folguera et al., 2002). The fault trace, is clearly recognized at the east of Llaima volcano, by the alignment of the Triful-Triful River and the scarp (~200 m height) between the Miocene granodiorites of the Melipeuco Plutonic Group and the Triful-Triful valley and can be followed passing east of Conguillío lake (Lara et al., 2008), towards the South of the volcanic edifice, the lineament of the Allipén River valley has been mapped (but not named) as a sinistral strike-slip fault (Melnick et al., 2006; Rosenau et al., 2006). The kinematics of the LOFZ result from a combination of dextral strike-slip and shortening across the arc, where the maximum compressional stress (σ_1) is NE while the minimum compressional stress (σ_3) is mostly sub-horizontal and NW (Cembrano and Lara, 2009). At the northern end (38-42°S) of the LOFZ, where Llaima is located, the deformation related structures, are described as arc-oblique and arc-parallel set of coeval synthetic (i.e. "C") and antithetic (i.e. "S") strike-slip faults, representing a SC-kinematics of deformation (Rosenau et al., 2006).

Llaima volcano is one of the most active volcanoes in Chile, with more than 50 eruptions since ~1650 CE (Petit-Breuilh, 2006). The foot print of the volcano covers an area of about 500 km² and comprises a main composite edifice that has two summits (3179 and 2920 m.a.s.l) and a set of about 44 scoria cones located on the mid-lower flanks. The predominant composition of the eruptive products is of a basaltic-andesite, although andesites and dacites have also been reported (Naranjo and Moreno, 2005; Ruth et al., 2016).

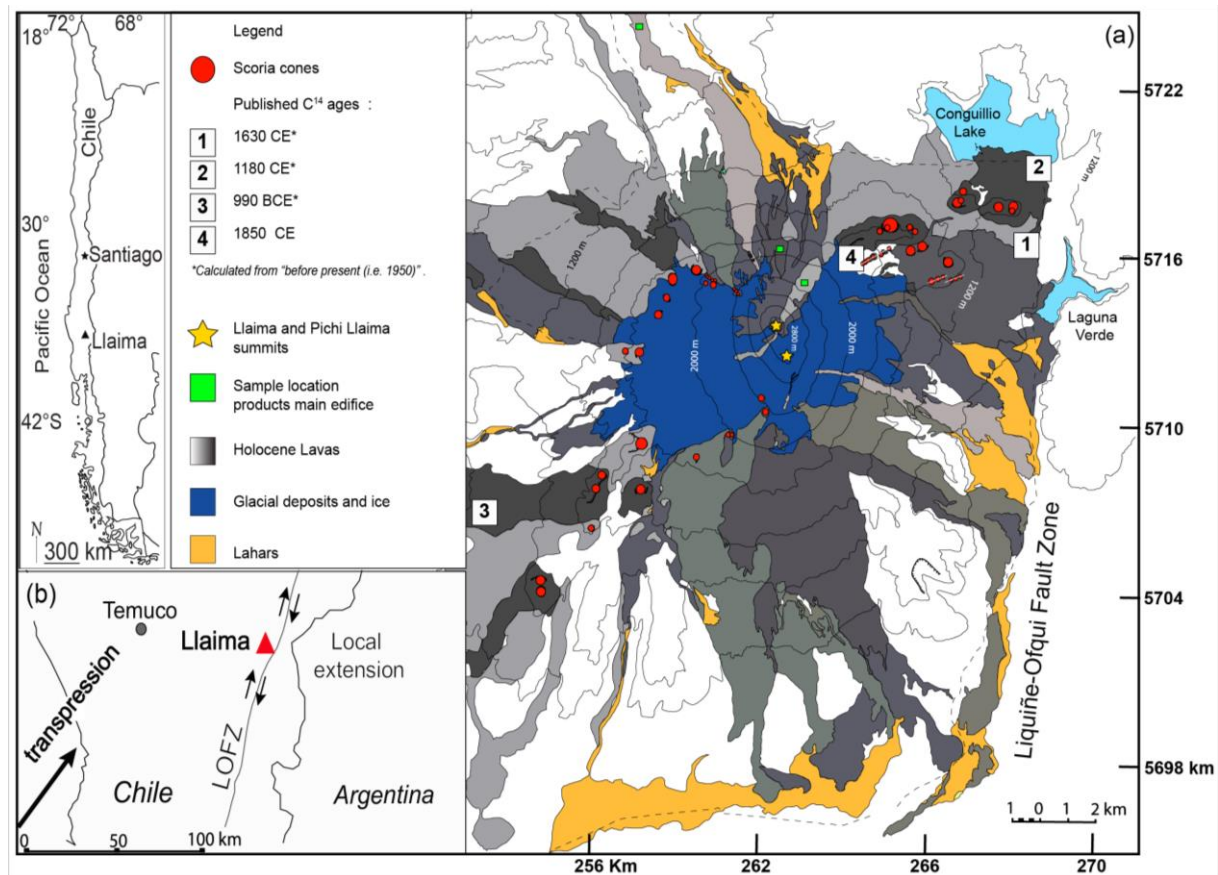


Figure 1. (a) Simplified geological Map of Llaima volcano, modified from Ruth (2014). Holocene lavas (grey scale), lahar deposits (orange) and glacial deposits and ice (dark blue) are shown. Red circles show the location of scoria cones. Numbers show the location of published C^{14} ages for the scoria cone eruptions; 1-3 from Naranjo and Moreno (2005) and 4 from Bouvet de Maisonneuve et al. (2012). (b) Regional tectonic context. Oblique transpression generated by the oblique subduction of the Nazca plate under the South American plate, creates local extension in the Liquiñe-Ofqui fault.

3. Methods

3.1 Individual study of the scoria cones

We studied the scoria cones as individual eruptions rather than as part of stratigraphic units (Schonwalder-Angel, 2015), as the majority of the cones are spatially disjointed, and the few ^{14}C ages previously published by Naranjo and Moreno (1991) and Bouvet de Maisonneuve et al. (2012) are insufficient to temporally constrain the entire eruptive stratigraphy (Fig. 1). Only

three scoria cone alignments at the NE flank, recognized by field- and remote sensing evidence, can be categorized as fissures. Regardless a detailed stratigraphy, the lack of erosion and relationship of the cones with glacial deposits suggests that the studied monogenetic activity at Llaima occurred between the Holocene and Recent.

We identified 44 individual scoria cones (Schonwalder-Angel, 2015), most likely monogenetic, using an ASTER image of the volcano area taken by NASA's Earth Observing - 1 Satellite using the Advance Land Image (ALI) on April 16th, 2009 (<https://earthobservatory.nasa.gov/IOTD/view.php?id=38271>; accessed: May 28, 2018). This image, complement with Google Earth® imagery were used to perform, for each cone, the measurement of the morphometric parameters proposed by (Tibaldi, 1995). At least one sample was collected from each of the 24 cones that were accessible to us during our field campaigns. Where possible, different eruptive products (i.e. scoria, spatter or lava) were sampled from different stratigraphic positions from individual cones, to identify if substantial differences exist within the products of a single eruptive event. Detailed information of the studied sample collection is reported in Schonwalder-Angel (2015) and the Supplementary Material 1, Table 1.

3.2 Textural analysis: Petrography and Crystal Size Distribution

Ninety samples (Supplementary material 1, Table 2), eight from the main volcanic edifice and 82 from its associated scoria cones, were selected for conventional petrographic descriptions (Schonwalder-Angel, 2015). Of these, 52 samples (4 from the main edifice) were selected for measuring the Crystal Size Distributions (CSDs) of the occurring main mineral phases: i.e. olivine, clinopyroxene, and plagioclase (Supplementary Material 2), using high-resolution back-scattered electron (BSE) images (~50 images per sample). The minimum magnification

per image was 300 μm , which allowed a cutoff to measure crystals bigger than 20 μm in diameter. The BSE images were collected using a Hitachi S-4000 scanning electron microscope (SEM) from the Instrumentation Center at the State University of New York at Buffalo. The collected images were analyzed using *ImageJ 1.45* open source software (downloaded from: <https://imagej.nih.gov/ij/>; accessed: May, 2018), in which the best-fit ellipse tool was used to estimate the long and short axes of the crystal sections. Between 300 and 500 measurements were performed per each phase to have a representative sample of each CSD. The mean crystal aspect ratios were estimated using the *CSD_output.ijm ImageJ* plugin. The data were then exported into *CSDCorrections 1.6* freeware, to calculate the CSD of each mineral phase (Higgins, 2006). Both plugin and freeware were downloaded from <http://www.uqac.ca/mhiggins/csdcorrections.html> (accessed: September, 2018). Additional parameters to calculate the CSD of a crystal population, such as the volumetric phase abundance and vesicularity of the samples, were determined using built-in features of *ImageJ*, while the total slide area was calculated by the addition of the individual areas of the used BSE images. All the calculated CSDs, their associated errors and their least square fitted regressions are reported in the Supplementary material 2. The residence time (τ) of a given crystal population was calculated using the expression

$$\text{slope} = - (1/G\tau) , \quad (1)$$

following Marsh (1988), where “slope” refer to the slope of the CSD and G is the crystal growth rate, assumed as constant and roughly equal to 10^{-10} [cm/s] following Cashman (1993).

3.3 Whole-rock chemistry

Forty-three lava and scoria samples, from the cones, were analyzed using X-Ray fluorescence spectroscopy (XRF) for major and trace elements while a subset of seventeen representative lava and scoria samples were analyzed for additional trace elements by inductively coupled

plasma mass spectrometry (ICP-MS; Supplementary Material 1, Table 3). Calibration standards used for XRF were RGM-1 and BHVO-1 (Gladney and Roelandts, 1988). For ICP-MS calibration, the standard used was JB-1 (Terashima et al., 1998). Accuracy of the data obtained is within $\pm 5\%$ on the basis of duplicate analyses for the BHVO-1 and JB-1 standards, detail for each element is tabulated in the supplementary material. All analyses were performed at the Department of Geological Sciences at Michigan State University, the methodology used can be retrieved at <https://ees.natsci.msu.edu/about/facilities/> (accessed: September, 2018). All whole-rock diagrams were generated using Vhub's online tool PINGU (Cortés and Palma, 2016).

3.4. Mineral chemistry

Mineral chemistry was determined on thirty-seven scoria and lava samples, from the scoria cones, using the electron microprobe (EPMA; Supplemental material 1, Table 4). We used the Cameca SX100 at the Laboratoire Magmas et Volcans, Clermont-Ferrand, France (<http://start.univ-bpclermont.fr/article7.html>; accessed on September 2018) and the JEOL 8900 Superprobe at the Cornell Center for Materials Research, Ithaca, USA (<http://www.ccmr.cornell.edu/instruments/jeol-8900-microprobe/>; accessed on September, 2018).

Working conditions in mineral phases in both instruments were 15 kV accelerating voltage, 15 nA beam current and a focused beam. Working conditions in glasses were obtained using 15 kV accelerating voltage, 4-8 nA beam current and a defocused beam (10-20 μm diameter). Peak counting times per element between 10 and 30s. Na_2O was analyzed first to minimize its mobility. Standards used for the Cameca SX100 were the San Carlos Olivine, Wollastonite, Forsterite, Fayalite Al_2O_3 , MnTiO_3 , Cr_2O_3 , Albite, Orthoclase, Apatite and NiO on blocks

provided by CAMECA or prepared at Clermont-Ferrand. Standards used for the JEOL 8900 where Olivine, Wollastonite, Albite, Apatite, from the block MINM25-53 manufactured by Astimex (<http://astimex.com>; accessed on September 2018). Detection limits for different elements vary according to the nature of the sample, the element concerned and the counting time, ranging from 0.2–0.5 wt % of elements. Accuracy is ± 1 wt% based on counting statistics, while precision in both instruments is >1 wt% based on 6 repeated analyses of the standards. Analyses with totals outside the 98–102 wt.% range were discarded for the purposes of this study. Calculations and plotting of the mineral chemistries were performed using Vhub's online tools: CFU (Cortés, 2015) and CFU-PINGU (Cortés, 2013).

3.5 Mass balance considerations and fractionation models.

Potential changes in the whole-rock compositions related to the fractionation of specific mineral phases were estimated using mass balance considerations, testing the feasibility of fractionation as the mechanism to explain the chemical variability between samples and groups. For major elements, the calculation was based on the lever rule, mineral chemistry, mineral proportions and stoichiometry to estimate the composition of the extract (Wilson, 1989; Cortés, 2009). Trace elements were extracted based in their partition coefficients (Rollinson, 1993) and the subtracted mineral proportion was estimated assuming Batch and Rayleigh fractionation models (Supplementary Material 3).

Calculations of fractionation models based on thermodynamic considerations were performed with rhyolite-MELTS (Gualda et al., 2012; Ghiorso and Gualda, 2015) using the intrinsic conditions reported by Ruth et al. (2016) for the Llaima system.

3.6 Scoria cone morphology and spatial distribution

The spatial orientation of individual dikes and the orientation of the principal components of the stress can be inferred by the morphology characterization of scoria cones following Tibaldi (1995). He defined nine morphometric parameters for scoria cones, grown in a sub-horizontal substrate ($<9^\circ$) that can be used to assess the orientation of magma feeding fractures. Three of those parameters are related (i.e. parallel) to the orientation of the feeder dike, therefore they can be used to assess dike orientations in cones grown in steeper substrate (Tibaldi, pers. comm.): the azimuth of fissures, coeval craters and crater elongation. The direction of cone breaching can be also linked to the orientation of the feeder dike but only on a sub-horizontal substrate. We used the ASTER image of the volcano and Google Earth® imagery, to outline the base and crater(s) of each cone, to determine the direction of the parameters mentioned above and identify which cones were emplaced in a sub-horizontal substrate.

4. Results

4.1 Two texturally distinct groups of scoria cones products

The main petrographic characteristics recognized in the studied rocks are presented in Figure 2. Based on these characteristics, we define two distinctive groups of cones whose samples (i.e. lavas, scorias and spatter) show distinct textural features. The first group is represented by eight scoria cones, of which we have collected 38 samples. The second group is represented by 16 scoria cones, with 44 collected samples. These characteristics are tabulated in Supplementary Material 1, Table 1.

The rocks from the first group are mainly characterized by the presence of glomerocrysts (~10%) of plagioclase and olivine, with some of the samples containing minor quantities of clinopyroxene. The presence of individual phenocrysts of subhedral to euhedral plagioclase

(~15%), subhedral to euhedral olivine (~7%) and subhedral clinopyroxene (~5%) is also characteristic. In all samples from the group, the phenocrysts and glomerocrysts are embedded in a plagioclase-clinopyroxene microlite-rich groundmass with traces of skeletal Fe-Ti oxide microlites. Phenocrysts appear as both, pristine and with disequilibrium textures. Olivine phenocrysts appear sub-rounded and commonly show embayments, while some clinopyroxene appear fractured and anhedral. Plagioclase phenocrysts display a wide range of disequilibrium features. Sieve textures are observed, either in the entire crystal, or constrained to its core and/or edge. Plagioclase zonation also shows a wide variability, from normal to oscillatory, the crystals can appear as simple euhedral twining crystals, or as subhedral with convoluted zonation patterns along the entire crystal or in parts of it. The disequilibrium textures recognized do not show any systematics associated with a specific cone or type (i.e. spatter, scoria and/or lava). Vesicle (~5%) show irregular shapes and variable sizes (10-100 μm). Similar chemical, mineralogical and textural characteristics found in this group of cones can also be found in products of the main volcanic edifice. For the purposes of this study, we will refer to this unit as the “glomeroporphyritic group”.

Samples from the second group are distinctive due to their microcrystalline nature containing plagioclase and clinopyroxene microlites as the main mineral phases. Fe-Ti oxides occur in some of the samples, and olivine appears as a minor constituent (~1%). Phenocrysts are nearly absent (~5%). The microlites of plagioclase and clinopyroxene are subhedral to euhedral, while the Fe-Ti oxides and olivine microlites are anhedral and can occur as skeletal crystals. Some samples show sparse and intensely altered phenocrysts of plagioclase, clinopyroxene and olivine. Vesicle content is relative higher (~10%), if compared with the glomeroporphyritic group, and they are characterized by their sub-rounded shape and relatively homogeneous sizes (~30 μm). These characteristics are observed in all the studied

lava and scoria products from the group and not obvious textural differences were observed between the two sample types. In this work, we refer to scoria cones whose products display these textures as the “pilotaxitic group”.

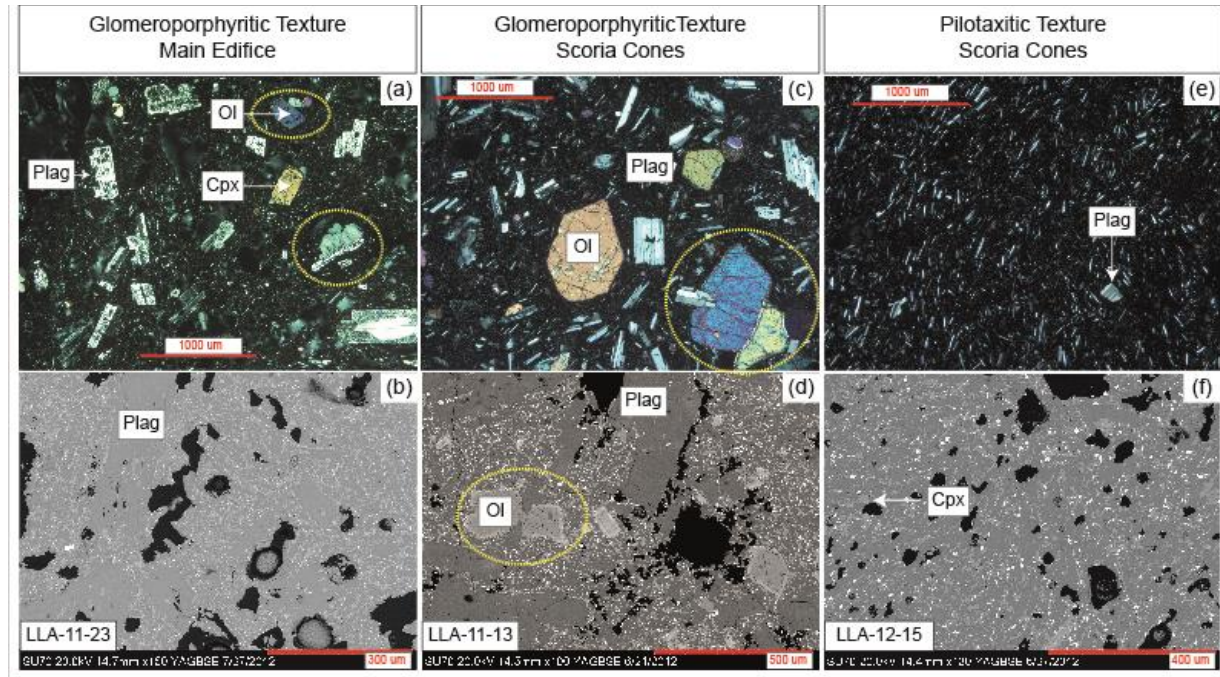


Figure 2. Photomicrographs and backscattered electron (BSE) images of the main textural characteristics for the described units. (a and b) Glomeroporphyritic textures observed in products from the main edifice. Olivine (Ol), clinopyroxene (Cpx) and plagioclase (Plag) phenocrysts are observed in a groundmass of glass, Plag, Cpx ferromagnesian and opaque microliths. (c and d) Glomeroporphyritic textures observed in one of the two scoria cone groups. Ol and Plag phenocrysts in a groundmass of glass, Plag, Cpx, ferromagnesian and opaque microliths. (e and f) Pilotaxitic textures observed in the other group of scoria cones. Volcanic glass and mainly Plag-Cpx microliths are identified. Yellow dashed-line areas show examples of glomerocrysts. LLA-11-23, LL-11-13 and LLA12-15 are the sample names. Scale bar in red. The area shown in BSE-images differ from the area shown in the photomicrographs.

For each sample selected for CSD analysis, the crystal size bins and the crystal population densities of the three main mineral phases were calculated using *CSDCorrections 1.6* (Supplementary Material 2). Those values were used to identify populations of crystals according to the changes (if any) from log-linear trends from the CSDs. For example, a concave-up CSD trend, would represent at least two populations, where the CSD fragment with a steeper slope represents populations of smaller crystals. We only accepted a crystal population, if the least-square fitted regression of the CSD fragment (i.e. slope) was between 0.97 and 1. All the CSDs from products of the studied scoria cones, as well as the main edifice, are summarized in Figure 3. Samples from historical lava flows, erupted from the main edifice in 1780 A.D., 1957 A.D. and in 2008 A.D. (Fig. 1), are characterized by kinked CSD trends of the olivine (max. crystal size: 0.6 mm) and plagioclase (max. crystal size: 0.8 mm) phases, while the clinopyroxene (max. crystal size: 0.15 mm) phase displays curved concave-up and log-linear CSDs. Similarly, the scoria, spatter and lava samples from the glomeroporphyritic group exhibit mainly curved and kinked CSD trends. Olivine trends are concave-up with maximum crystal sizes up to 1.2 mm. Clinopyroxene shows both log-linear and concave-up CSD with a maximum crystal size around 0.3 mm. Plagioclase shows kinked and concave-up CSD and maximum crystals sizes up to 1.2 mm. The CSDs of these three main mineral phases, in the pilotaxitic group, exhibit mainly log-linear trends and relatively smaller crystals (up to 0.4 mm).

For each recognized crystal population, a residence time was calculated using equation 1. The values of the maximum and minimum population densities (i.e. error bars; Supplementary Material 2) that are provided by *CSDCorrections 1.6*, were used to find the maximum and minimum slopes possible for each CSD fragment, and hence to calculate the time range possible for each crystal population (Supplementary Material 2, tabs 1 and 2). Figure 4 shows

a compilation of the maximum residence times for the main mineral phases, according to the textural groups here studied. The rocks of the glomeroporphyritic group show longer residence time for the olivine (up to 12 ± 0.6 years) and plagioclase (up to 12 ± 2.4 years) phases. Conversely, the rocks of the pilotaxitic group show shorter residence time for the same phases; up to 6 ± 0.2 years for olivine and 4 ± 0.1 years for plagioclase. No clear distinction is observed in the calculated residence times for the clinopyroxene phase, in both groups the maximum residence time is up to 2 ± 0.1 years. Along similar considerations, the calculated residence times do not seem to be controlled by the nature of the volcanic products, as scorias and lavas in each respective group show similar residence times.

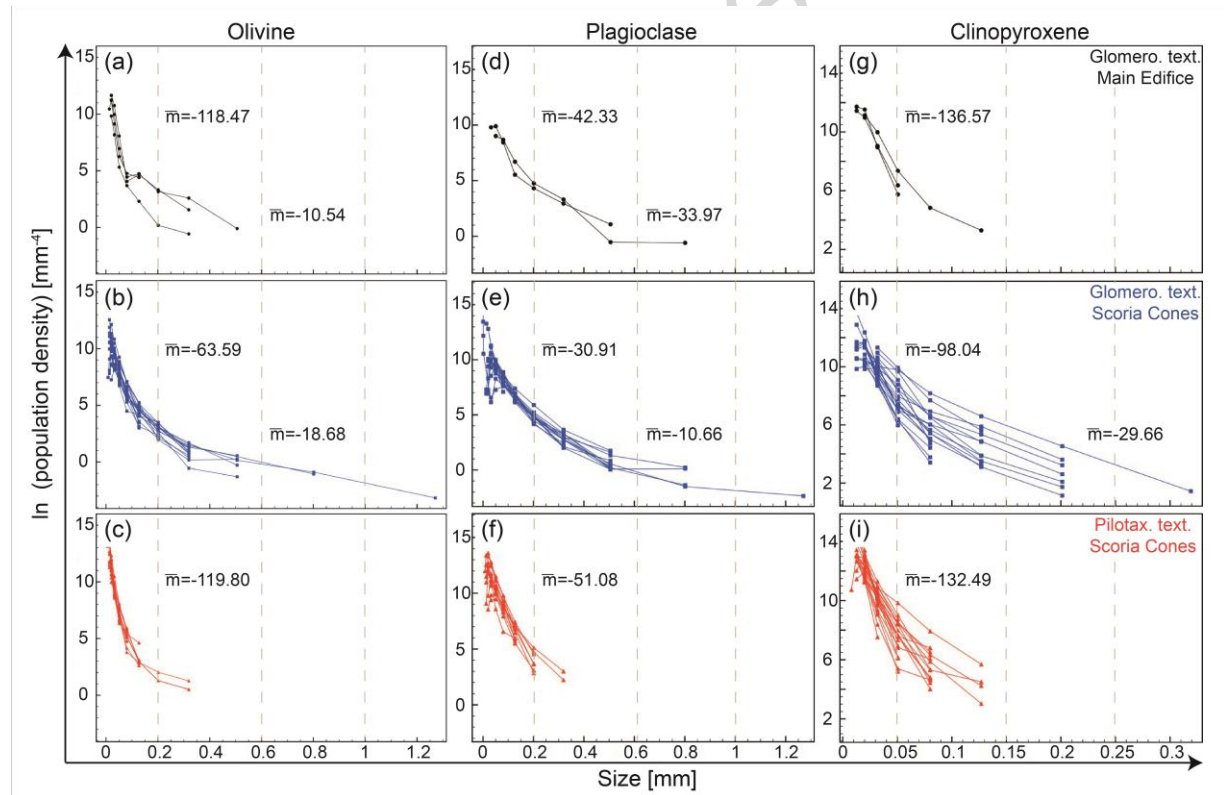


Figure 3. Crystal Size Distribution (CSD) of main mineral phases. (a,b and c) Olivine CSDs for products from the main edifice, and the scoria cone groups with glomeroporphyritic and pilotaxitic textures. (d,e and f) Plagioclase CSDs for the products of the same three groups (g, h and i) Clinopyroxene CSDs for the products of the same three groups. The left truncation

(lower size limit) of the CSDs is the smallest size that could be measured. \bar{m} Represents the average of the slope of CSD trends.

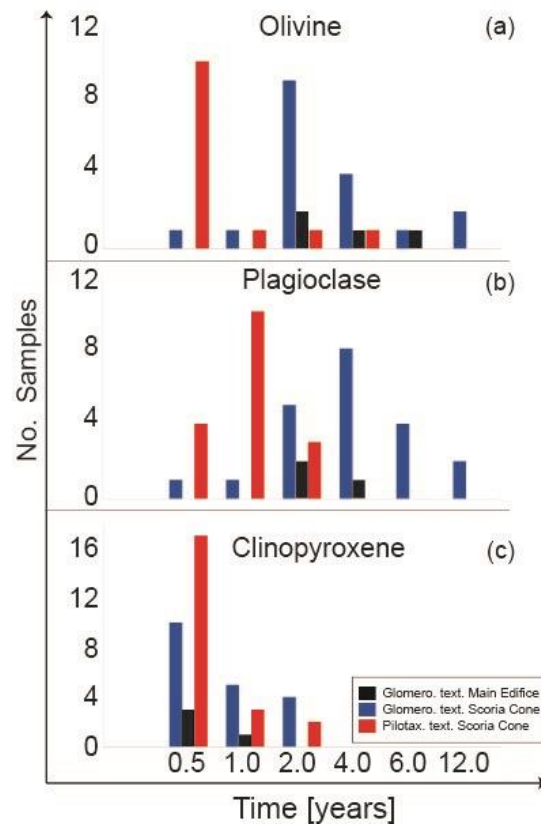


Figure 4. Histogram of maximum residence time (in years), for the main mineral phases in each studied group. (a) Olivine phase. (b) Plagioclase phase. (c) Clinopyroxene phase.

4.2 Whole-rock chemical compositions

Whole-rock chemical analyses are reported in Schonwalder-Angel (2015) and summarized in the Supplementary Material 1, Table 3. In a Total Alkali vs. Silica (TAS; Fig. 5) diagram (LeMaitre et al., 2002), the studied samples are calc-alkaline basalts and basaltic-andesites, within the field of the compositions previously reported at Llaima volcano (Naranjo and Moreno, 1991; Ruth et al., 2016). Clear distinctions between the two textural groups are observable in major and trace elements whole-rock chemistry (Figs. 6 and 7). Overall, samples from both groups show positive correlations between SiO_2 and TiO_2 , FeO , Na_2O , K_2O and P_2O_5 , and negative correlations between SiO_2 and Al_2O_3 , MgO and CaO . However, samples

from the glomeroporphyritic group have less evolved compositions (51-55 wt% SiO_2) than the pilotaxitic group (55-60 wt% SiO_2 ; Figs. 5 and 6). Relative lower contents of Na_2O (2.9-4.0 wt%) and K_2O (0.5-0.8 wt.%), with relative higher contents of MgO (4.1-6.1 wt.%), CaO (8-11 wt.%) and Al_2O_3 (16.5-18.7 wt.%) are also recognized in the glomeroporphyritic group. Considering some petrogenetic-relevant trace elements, the distinction between both groups is evident as the glomeroporphyritic group shows higher Ni (up to 55 ppm; Fig. 7a) and Cr (p to 110 ppm; Supplementary Material 1, Table 3) compared with the Pilotaxitic group (Ni up to 45 ppm; Cr up to 80 ppm). In a diagram of Ni/Rb vs. Rb (Fig. 7a) it is clear that samples from the glomeroporphyritic group contain, in absolute terms, larger amounts of compatible elements than the Pilotaxitic group. On the other hand, in a diagram of $\text{K}_2\text{O}/\text{Rb}$ vs Rb (Fig. 7b), it is clear that the ratio between incompatible elements is in practical terms constant.

In a REE element diagram (Fig. 7c), similar patterns (relative enrichment of the LREE compared with the HREE with variable Eu anomaly) are consistent with a common origin with a variable degree of fractionation. The spider diagram (Fig. 7d) is compatible with this interpretation. In this diagram, we observe that both groups show decoupling between LIL and HFS elements, with LIL elements enriched compared to N-MORB. Positive anomalies are also observed in Ce and Sm, with Ce being the most pronounced.

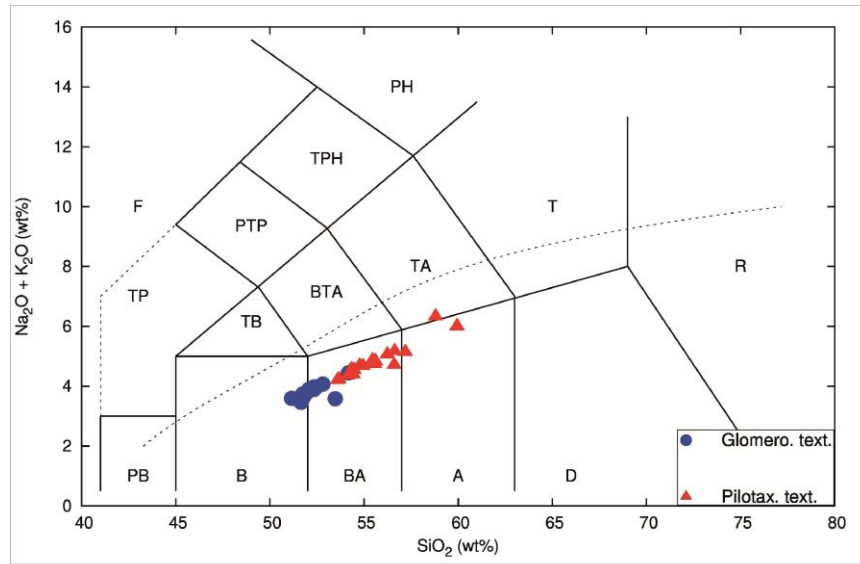


Figure 5. (a) Total Alkali-Silica (TAS) diagram after LeMaitre et al. (2002). Blue circles: samples from the glomeroporphyritic group, Red triangles: samples from the pilotaxitic group. Dashed line shows the boundary between alkaline and sub-alkaline series (Irvine and Baragar, 1971).

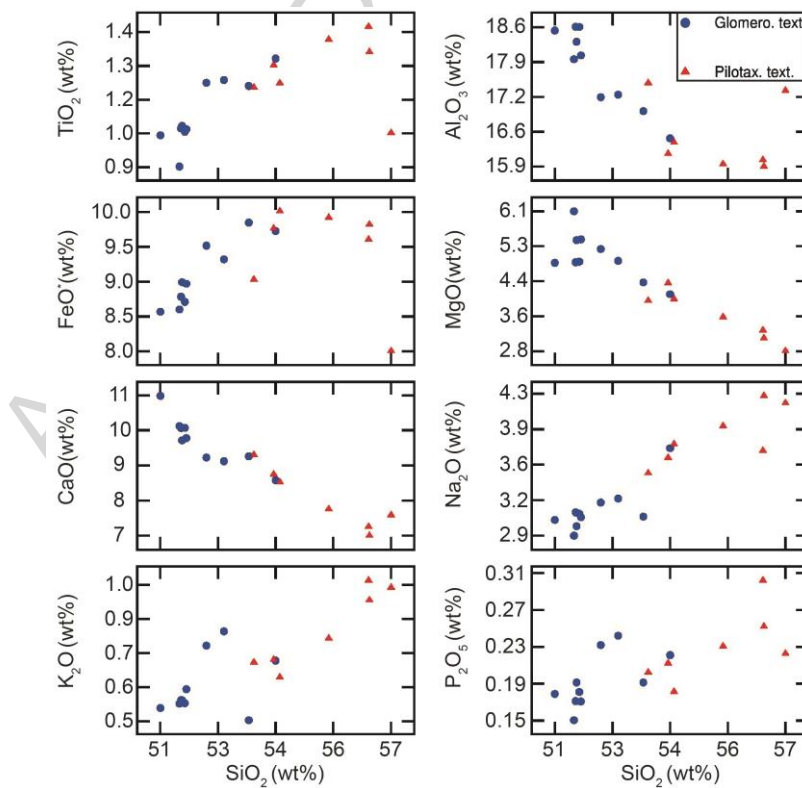


Figure 6. Variation diagrams of major-element oxides vs. SiO_2 (wt. %) for the different studied groups. Symbols as in Figure 5. $\text{FeO}^* = 0.8998 \times \text{Fe}_2\text{O}_3^*$

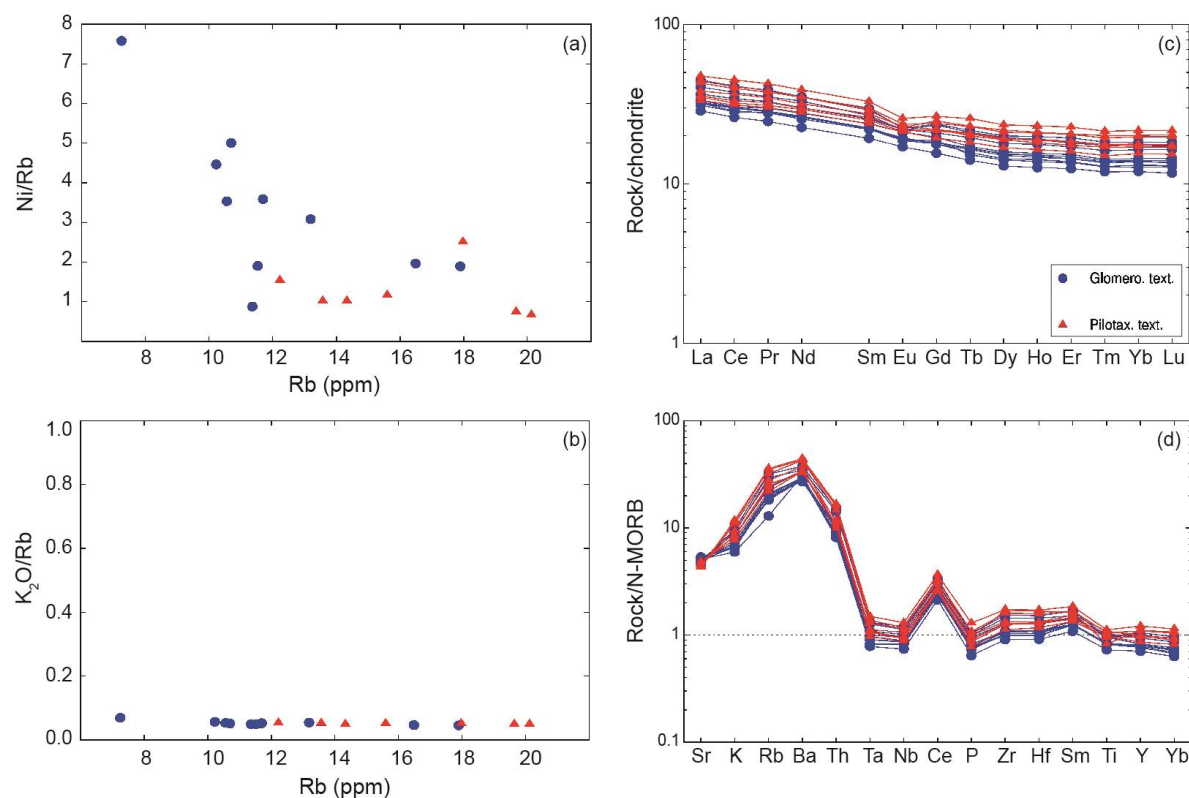


Figure 7. (a) Ni/Rb vs Rb (ppm) variation diagram. (b) $\text{K}_2\text{O/Rb}$ vs. Rb (ppm) variation diagram. (c) REE diagram normalized to chondrite. (d) Multi-element diagram (spider diagram) normalized to N-MORB. Abundances normalized to C1 chondrite values and N-MORB values from Sun and McDonough (1989). Symbols as in Figure 5.

4.3. Mineral chemistry

Classification diagrams for plagioclase, olivine, and pyroxene phases are shown in Figures 8a,b,c respectively. Mineral chemistry analyses are reported in the Supplementary Material 1, Table 4 and by Schonwalder-Angel (2015). The most noticeable difference between the two groups is observed in the plagioclase phase, showing a wider range of compositions (An_{50-90}) in the glomeroporphyric group than in the pilotaxitic group (An_{55-70}). Plagioclase analyses from the main edifice show a similar compositional spread than those in the

glomeroporphyritic group. Olivine in the glomeroporphyritic group show a wider range of compositions (Fe_{50-80}) than in the pilotaxitic group (Fe_{60-65}) and the main edifice (Fe_{70-80}); and both, the glomeroporphyritic and main edifice olivine compositions are richer in Mg if compared with the olivine from the pilotaxitic group. Augite (Mg# 55-94 in the glomeroporphyritic group and Mg# 63-83 in the pilotaxitic group) is the main pyroxene phase occurring in all the studied samples, although pigeonite and enstatite-pigeonite are also recognized as a minor component in the groundmass of all the groups.

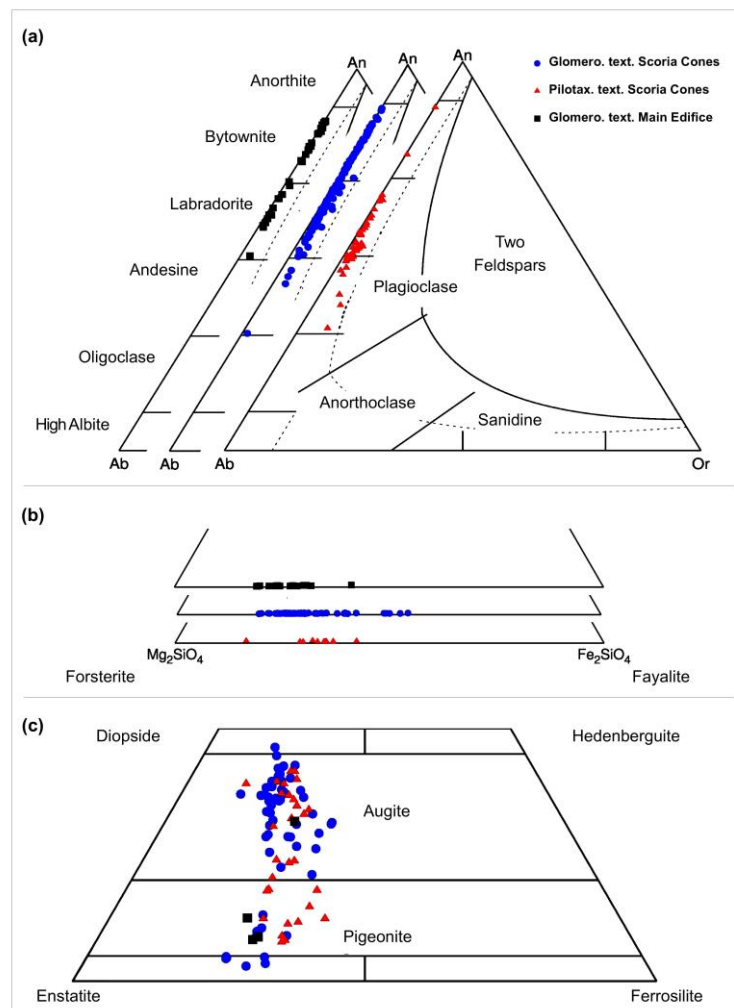


Figure 8. (a) Plagioclase classification diagram in terms of the end-members Anorthite (An), Albite (Ab) and Orthoclase (Or) for phenocrysts and groundmass in the two groups and in the main edifice products. Plagioclase diagram after (Deer et al., 1992). (b) Compositions of olivine in terms of end-members Forsterite and Fayalite (c) Pyroxene quadrilateral

classification diagram in terms of the end members: Diopside-Hedenbergite, Enstatite-Ferrosilite (Morimoto, 1989). Black squares: Glomeroporphyritic samples from the main edifice. Blue circles: samples from the glomeroporphyritic group. Red triangles: samples from the pilotaxitic group.

4.4 Mass balance constrains and Fractional Crystallization models

In the following, we will first show that pilotaxitic products can be easily derived from the whole-rock glomeroporphyritic products by the direct removal of the main occurring mineral phases. As already shown, products from the pilotaxitic group are consistently more evolved ($\text{SiO}_2 \sim 53\text{-}57 \text{ wt } \%$) than those from the glomeroporphyritic group ($\text{SiO}_2 \sim 51\text{-}53 \text{ wt } \%$). In the variation diagrams (Fig. 6), linear trends between SiO_2 and MgO , Al_2O_3 , CaO , Na_2O and K_2O could represent a mixing trend between two compositional end-members or a process of mineral fractionation, starting from the most primitive composition in the diagram. A preliminary basic exploration of the data was performed following Pearce's elemental ratio approach (Pearce, 1968; Nicholls, 1988; Nicholls and Russell, 1990). The data trend (Fig. 9) is strongly consistent with fractionation of plagioclase + olivine with minor fractionation of clinopyroxene, in agreement with the average petrography of both groups (i.e. glomerocryts of mainly plagioclase and olivine in the glomeroporphyritic group and lack of these in the pilotaxitic group).

Using olivine Fo_{60} , plagioclase Ab_{80} and clinopyroxene $\text{Mg}\# = 75$ compositions, extracted in the proportion 60% plagioclase + 20% olivine + 20% clinopyroxene from the melt, satisfactory fractionation trends for Al_2O_3 , CaO and Na_2O can be reproduced (Figs. 10b,c,e). Elements like MgO and TiO_2 (Figs. 10a and 10d) depart from the trend at around 55% of SiO_2 , suggesting the additional removal of titanomagnetite at more evolved compositions. In

an analogue way, P_2O_5 (Fig. 10f) does not follow a fully incompatible trend implying that apatite is in the fractionated assemblage.

These constraints are also consistent with mass balance in the REE whole-rock chemistry, in which pilotaxitic trends (Fig. 7c) are consistently displaced upwards with a well-defined Eu anomaly when compared with samples from the glomerophyritic group. A simple batch fractionation approach, using Rollinson (1993) compilation of partition coefficients, shows that this can be well achieved by fractionating 70% of plagioclase, 20% of olivine and 10% of clinopyroxene starting from a glomerophyritic sample (sample LLA-12-25, Fig. 12; Supplemental material 3). A Rayleigh fractionation mechanism, while accurate at modeling the LREE elements, produces a more depleted pattern for the HREE elements (Supplemental material 3). This result shows that pilotaxitic REE compositions could be derived from glomerophyritic composition by one, single batch removal event.

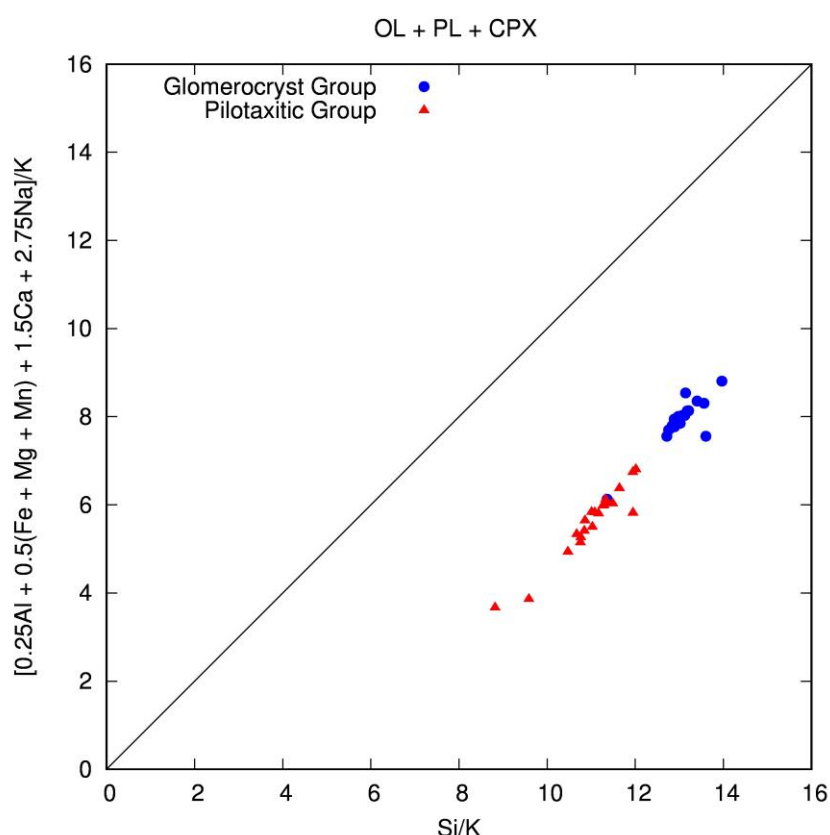


Figure 9. Pearce Elemental Ratio diagram constructed to follow the fractionation of olivine, plagioclase and clinopyroxene according to Nicholls and Russell (1990), i.e. fractionation of these phases should follow a straight line with slope 1. Blue circles, Glomeroporphyritic Samples, Red Triangles, Pilotaxitic samples. Black solid line is the 1:1 line.

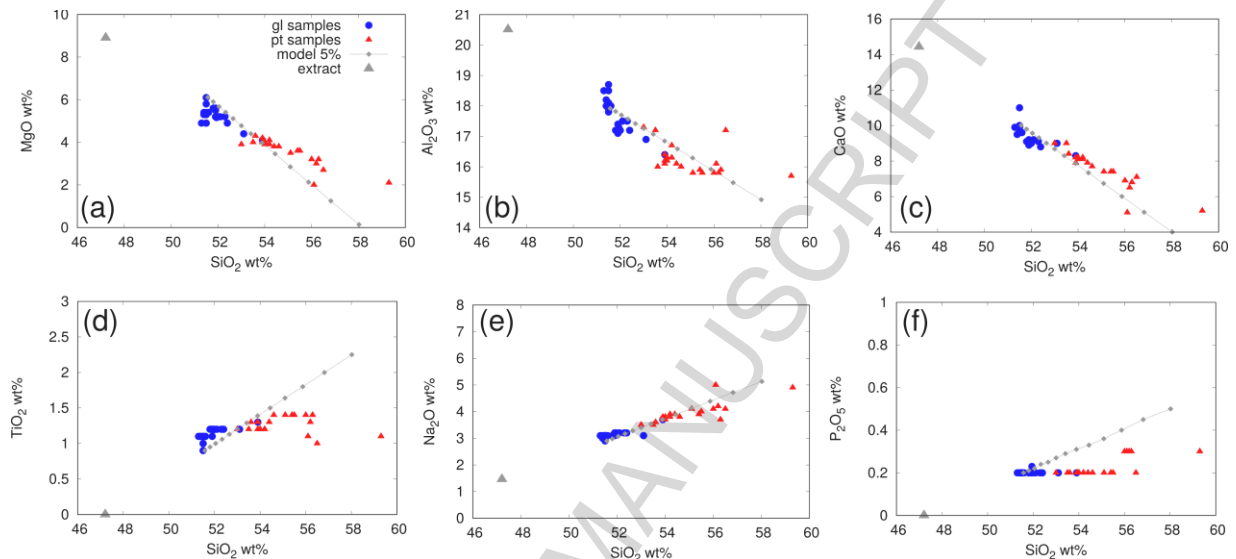


Figure 10. Variation diagrams of MgO (a), Al_2O_3 (b), CaO (c), TiO_2 (d), Na_2O (e) and P_2O_5 (f) versus SiO_2 . Blue circles: Glomeroporphyritic samples, red triangles: Pilotaxitic samples. The grey line is the compositional change occurring by subtracting in decrements of 5% olivine, plagioclase and clinopyroxene in the proportion and compositions given in the text (Black triangle is the composition of the overall extract) to sample LLA-12-52B. See text for more details.

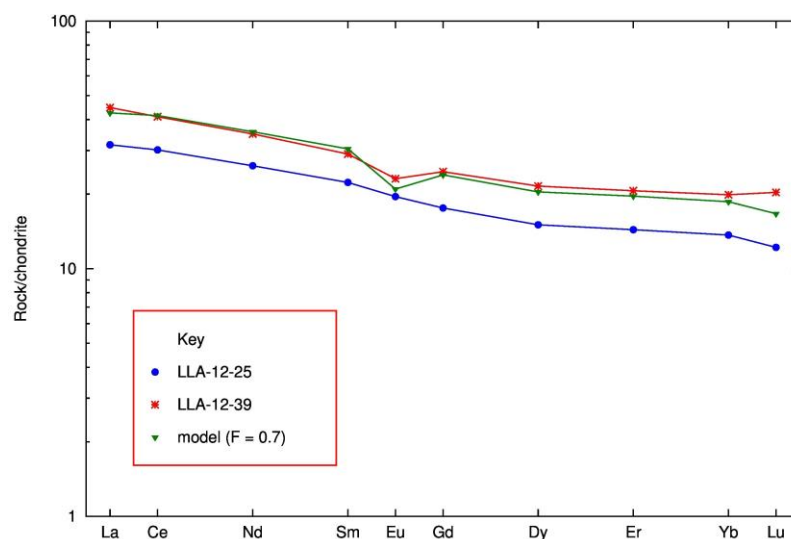


Figure 11. REE diagram for sample LLA-12-25 (blue circles and line; glomeroporphyritic group) and sample LLA-12-39 (red stars and lines; pilotaxitic group). Model (green triangles and lines) was obtained with a batch fractionation process, starting from sample LLA-12-25, with F (weight fraction) = 0.7 and fractionation of 70% plag, 20% ol and 10% of cpx. Samples normalized according C1 chondrite of Sun and McDonough (1989). See supplementary material 3 for details.

4.4.1 MELTS calculations

To assess the thermodynamical feasibility of a fractional crystallization process based on the mass balance considerations described in the previous section, we used the widely accepted rhyolite-MELTS model (Gualda et al., 2012; Ghiorso and Gualda, 2015). We performed the calculations using again, as starting composition sample LLA-12-52B, assuming an oxygen fugacity equivalent to Nickel-Nickel Oxide buffer, typical of arc volcanoes (Toplis and Carroll, 1995). We also considered pressures at 50, 100 and 342 MPa and temperatures between 1094-1233°C (calculated from Olivine-melt equilibrium) and 1109-1167°C (calculated from Plagioclase-melt equilibrium), following the work of Ruth et al. (2016) at Llama volcano.

Figure 12 shows on selected variation diagrams, five isobaric liquid line of descent calculations, performed at 10, 50 100, 200 and 340 MPa. Initial temperature was set at 1150°C and the option of fractionating the crystallizing solids was turned on. Glomeroporphyritic and Pilotaxitic analyses shown in Figure 6 have also been plotted in the diagrams. Consistent with the mass balance constrains, there is a fair agreement between the low-pressure calculations and the samples from both groups, except for P_2O_5 , which rhyolite-MELTS models as an incompatible element (Fig. 12f).

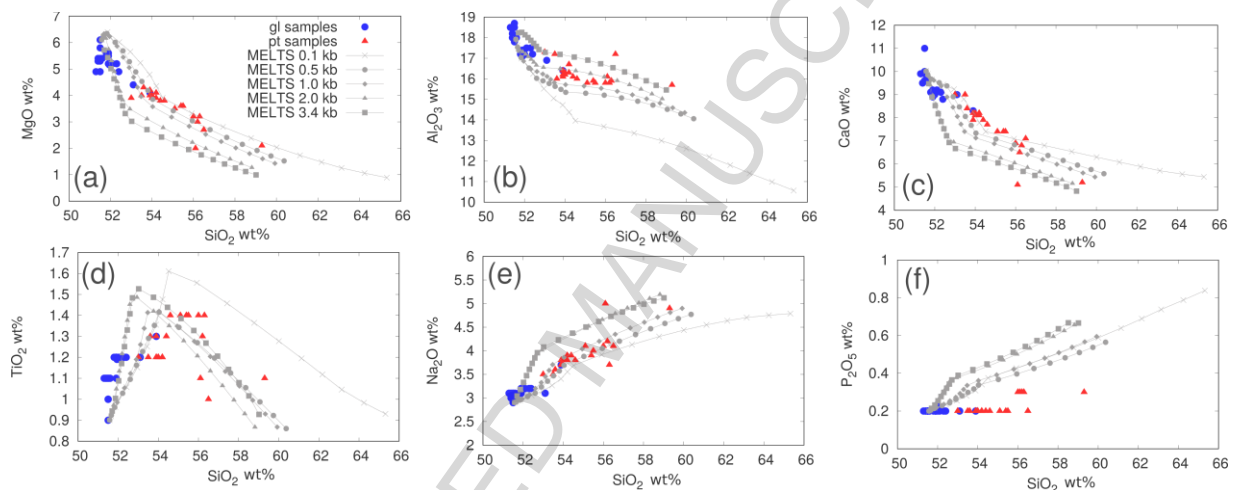


Figure 12. Variation diagrams of MgO (a), Al_2O_3 (b), CaO (c), TiO_2 (d), Na_2O (e) and P_2O_5 (f) versus SiO_2 . Blue circles: glomerocrystic samples, red triangles: pilotaxitic samples. Grey lines are the calculated fractionation paths at different pressures (see key) using the rhyolite-MELTS model (Gualda et al., 2012; Ghiorso and Gualda, 2015). See text for details on the intrinsic parameters used as initial conditions in the calculations.

4.5 Scoria cones morphology and their spatial distribution in a tectonic context.

Figure 13a shows the location of the glomeroporphyritic and pilotaxitic scoria cones and the location and type of samples collected. Figure 13b shows the morphology parameters of the cones, and the main tectonic features around Llaima. Regardless the group, all the scoria

cones are in the NE, NW and SW flanks of the main edifice. At the SE flank, no scoria cones were recognized, just a few lava-feeding vents. Some cones at the SW flank were assumed to be part of the pilotaxitic group, due to the characteristics of the lava samples collected in the lower flanks, even if the source cones were not sampled. A few cones in the NW and SW flanks were not categorized as part of any of the groups, due to lack of stratigraphic context. Cones that are in the glomeroporphyritic group are mainly located in the NE flank, including three fissures. One cone from this group was recognized at the SW flank. Cones in the pilotaxitic group were recognized in the NE, NW and SW flanks.

The morphology parameters measured (Fig. 13 b,c) are tabulated in the Supplementary Material 1, Table 5. We were able to measure two key parameters, the orientation of fissures (azimuth 60° - 75° NE) and elongated craters (azimuth 5° - 70° NE) in cones from the glomeroporphyritic group. The azimuth of cone breaching, for cones of both groups, shows a wider range of orientation towards the NE and NW, probably as a result of cones being emplaced on a substrate inclination equal or larger than 9° . Conversely, no fissures were recognized in the pilotaxitic group, just one elongated crater with an azimuth of about 315° NW. We can infer that the main orientations for the glomeroporphyritic feeding dikes are towards the NE, parallel to the regional σ_1 . For the pilotaxitic feeder dikes, a clear orientation of the dikes cannot be assumed, due to the lack of fissures and statistically significant measurements of crater elongation. Nevertheless, their spatial distribution on the NE, NW and SW flanks, suggest a radial-to-the-edifice pattern. The SE flank, where the cones are absent, is the closest area to the intersection between the two main faults in the area.

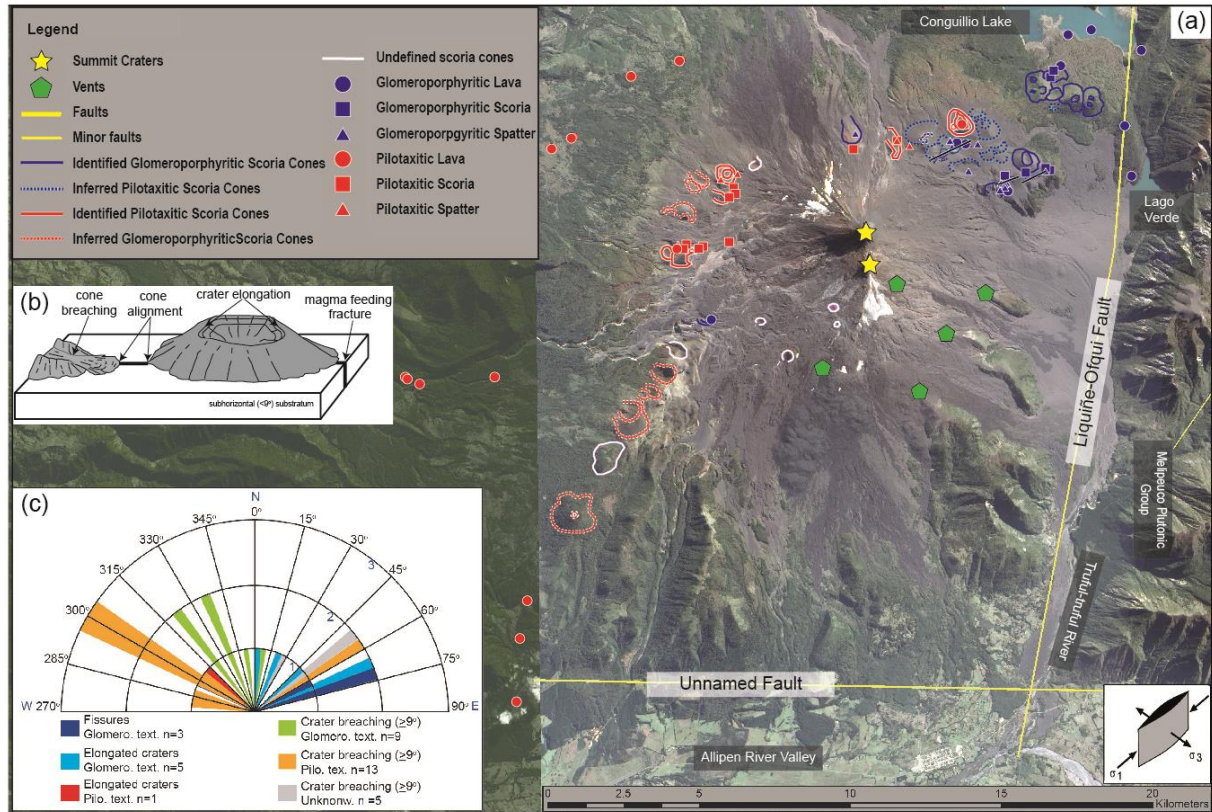


Figure 13. (a) Spatial distribution of scoria cones according to group classification. Solid blue lines outline the base and crater(s) of cones from the glomeroporphyrritic group. Dashed blue lines represent cones that we infer as part of this group. Red solid lines outline the base and crater(s) of cones from the pilotaxitic group. Dashed red lines represent cones that we infer as part of this group. The main structures in the area are also shown. Inset shows the orientation of the regional stress. Llama image taken by NASA's Earth Observing -1 Satellite (ALI) on April 16, 2009. (<https://earthobservatory.nasa.gov/IOTD/view.php?id=38271>). (b) Schematic diagram showing the morphology parameters of scoria cones measured that are linked to the orientation of the magma feeding dikes. Modified from Tibaldi (1995). (c) Rose diagram showing the azimuth distributions for the morphology parameters measured for each cone.

5. Discussion

Beginning with the recognition of a common source for all Llaima magmas (e.g. Figs. 7c,d), likely the depleted mantle in the subduction wedge (Tormey et al., 1991; Hickey-Vargas et al., 2016), any chemical, textural and mineralogical variation between the different volcanic products is a later consequence of processes occurring within the volcanic plumbing system. In the following, we evaluate these variations in detail, particularly assessing them in the context of the structural controls dictating the geometry of the plumbing system.

As we have clearly shown in our results, based on chemical, textural and mineralogical differences, there are two distinctive groups of satellite cones, occurring around the volcanic edifice at Llaima. We have named them “glomeroporphyritic” and “pilotaxitic” groups based primarily in the textures and mineralogy observed in their products. Because of the resolution of our data, it is not possible to generate a detailed stratigraphy of the eruptive sequence of the cones and their relationship with the central edifice lavas, with aims to identify any variation that might be temporally-controlled. It is however reasonable to assume that these variations *are not an evolutionary trend in the system* (i.e. different products erupting at different times), because all the studied monogenetic activity is only restricted to the Holocene/Recent activity (Naranjo and Moreno, 2005; Bouvet de Maisonneuve et al., 2012). The fact that volcanic products sourced from the main edifice are only similar to the glomeroporphyritic cones, and that the variations are clearly spatially-controlled, also support this assumption.

Although, it is unlikely than an evolutionary trend explains the described variations, our results clearly show that the feeder magmas for the pilotaxitic cones can be directly derived from the glomeroporphyritic-sourcing melt by fractional crystallization of olivine, plagioclase and minor amounts of clinopyroxene. Lines of evidence for this are chemical, textural and mineralogical.

Compositions of the glomeroporphyritic cones are more primitive than the compositions of the pilotaxitic cones, having higher contents of MgO, Ni and Cr than those (Figs. 6 and 7), reflecting the mafic character of the source (Cortés et al., 2005; Schmidt and Gruner, 2011). The variation between both types of cones is strongly consistent with mineral fractionation as shown in the trend generated in a PER diagram designed to follow specifically the fractionation of olivine, plagioclase and clinopyroxene (Fig. 9), and any mass balance considerations between samples from both groups (Figs. 10a-f). In close agreement with these variations in whole-rock chemistry of major elements, fractionation of olivine, plagioclase and minor amounts of pyroxene could also produce the variations observed in trace and REE elements (e.g. Figs. 7c,d) and the overall variation of compatible elements (e.g. Ni; Fig. 7a) by a batch-fractionation process. Fractionation is also consistent with the paucity of changes in incompatible element ratios comparing samples from both groups (e.g. Fig. 7b).

In terms of textural variations, troctolitic glomerocrysts are a clear evidence of early crystallization from a primitive magma, while pilotaxitic textures can be interpreted as consequence of removal of phenocrysts and glomerocrysts in a single fractionating event followed by groundmass crystallization prior to eruption. From a textural point of view, this can also be inferred due to their rare occurrence in pilotaxitic products (<2%; Fig. 2). We interpret the presence of glomerocrysts (Fig. 2) the remnants, of both, the cumulate layers disrupted by the influx of new magma into the reservoir and from the recharge itself (Browne et al., 2006; Jeffery et al., 2013). When magma recharge occurs, multiple crystal populations are combined and some of them develop textural discontinuities such as zonation patterns and/or resorption features (Streck, 2008; Sparks and Cashman, 2017). Multiple crystal populations (e.g. curved-kinked CSDs; Fig. 3) with variable residence times (Fig. 4) are

consistently recognized in the glomeroporphyritic rocks. Plagioclase and olivine crystals appear zoned and with sieve and embayment textures (Fig. 2).

Groundmasses in samples from both groups show distinctive plagioclase-clinopyroxene microlite-rich textures, unimodal crystal populations (i.e. log-linear CSD trends in the pilotaxitic samples and in the small crystal sizes in the glomeroporphyritic samples; Fig. 3) and relative shorter residence times (Fig. 4). Groundmasses in both cases can be interpreted as the result of magmatic decompression and volatile exsolution processes prior eruption, as the observed crystal sizes and lack of disequilibrium features imply high undercooling of the system with episodes of crystal growth at equilibrium with a degassing melt (Marsh, 1988; Szramek et al., 2006).

Closely related with the textural patterns and the distribution of crystal populations are the compositional range observed in the mineral chemistry. The narrower range of compositions in olivine and plagioclase in the pilotaxitic group (Fo₆₀₋₆₅; An₅₅₋₇₀) can be considered an evolved subset of the wider range of compositions observed in the glomeroporphyritic group (Fo₅₀₋₈₀; An₅₀₋₉₀). This is not observed in the clinopyroxene phase, in which the range of Augite compositions in terms of Mg# is similar in both groups, consistent with a minor role of this phase in the fractionating event, likely related with a later crystallization of this phase.

We have also observed that products from the glomeroporphyritic group *are textural, compositionally and chemically identical* than the studied products erupted from the main volcanic edifice, suggesting that the conditions and processes of the main Llaima system are the same conditions and processes controlling the mineralogy and chemistry of the dikes sourcing these cones. Indeed, Ruth et al. (2016) and Bouvet de Maisonneuve et al. (2012),

pointed out that this volcanic system is constantly fed by a basaltic recharge. Using the most primitive sample from the glomeroporphyritic group and the intrinsic values reported by Ruth et al. (2016) as input values, rhyolite-MELTS (Gualda et al., 2012; Ghiorso and Gualda, 2015) reproduces the trend between the two groups at relatively shallow conditions (i.e. pressures of 100 MPa or less) and temperatures in the range of 1150-1100, implying that the fractionation process that generates the pilotaxitic melts must have occurred within the volcanic edifice/plumbing system. Although not much work has been done on the thermodynamic properties of apatite (Biggar, 1966; Green and Watson, 1982), the discordant behavior of P_2O_5 between model and data can be attributed to the actual water mobility in the system (Green and Watson, 1982), suggesting that the volatile phase is a relevant variable in the fractionation process. Changes in the conditions of the volatile phase, could be also the main trigger of apatite crystallization in some of these melts (Green and Watson, 1982).

In summary, all the described characteristics and variations, seem to be easily explained by magma recharge and mixing producing a hypothetical common source (i.e. glomeroporphyritic group), which in some cases follows a further, simple, single (batch) event of fractionation (i.e. pilotaxitic group), and that this process occurs at shallow levels. It follows that the conditions in the plumbing system are then the key controlling factor for a fractionation process (Roman and Jaupart, 2014). We now explore in detail these conditions.

Large edifices (~2500 m) induce stresses in its substrate that can exceed the critical reservoir overpressure. This influence decreases horizontally and in depth over distances twice the edifice radius (~5-15Km). As a result, in the focal area, vertical propagation of magma is hindered allowing differentiation (Roman and Jaupart, 2014). Based in all the constrains previously described, the dimension of Llama's volcanic edifice and the control exerted by the regional tectonics, we proposed that both groups of scoria cones are fed by dikes that

initiate at the same source and that propagate radial to the volcanic edifice, however glomeroporphyritic dikes, aided by an extensional tectonic control, propagate unimpeded to the surface (Cembrano and Lara, 2009). Consequently, glomeroporphyritic products reflect more primitive magmas compared with the fractionated products from the pilotaxitic group. The lack of scoria cones at the SE, on the other hand, represent crustal compressional stresses that obstruct dike emplacement.

From a regional perspective, is well known that the regional tectonics of the SSVZ where Llaima is located, is characterized by a maximum compressional stress (σ_1) trending NE while the minimum compressional stress (σ_3) is mostly sub-horizontal and NW (Nakamura, 1977; Cembrano and Lara, 2009). The crustal tectonic deformation is further affected by the SC-kinematics of deformation at the northern part of the LOFZ (Rosenau et al., 2006). Figure 14a shows the overall inferred orientation for the feeder dikes, based in the morphometric parameters (Fig. 13) of the pilotaxitic and glomeroporphyritic scoria cones, as well as the orientation of the regional stress. Figure 14b and 14c show the SC-kinematics crustal deformation model proposed by Rosenau et al. (2006) and our proposed location of the Llaima edifice with respect to their model. The main faults identified around Llaima, remarkably agree with the location of the faults within the SC-kinematic model of deformation, where the synthetic (i.e. C) fault is represented by to main trace of the Liquiñe-Ofqui fault, and the Allipén River lineament represents the antithetic (i.e. S) fault. In this model, Llaima is located in one of the extension quadrants of the theoretical ellipse of deformation (Fig. 14c).

The spatial distribution of the cones and the inferred orientation of their feeder dikes, suggest that all the dikes are emplaced in a radial-to-the-edifice pattern, in agreement with the

expected trajectories of dikes influenced by the load of a volcanic edifice (Roman and Jaupart, 2014). However, the glomeroporphyritic feeder dikes are exclusively oriented towards the NE, parallel to the regional σ_1 , and normal to the axes of extension according to model of Rosenau et al. (2006). At the SE flank, the lack of scoria cones, coincides with an area of crustal folding generated by the interaction between the dextral and sinistral faults (Rosenau et al., 2006). Hence, our proposed model, where an interplay of local crustal stresses imposed by the volcanic edifice and the regional tectonics define the emplacement of dikes that initiated in the same source, is supported. Glomeroporphyritic dikes emplacement is then facilitated by local extensional deformation, which allows more magma flux (van Wyk de Vries and Merle, 1998), whereas, the radial emplacement of the of the pilotaxitic dike, is controlled by the edifice loading, that enables mineral fractionation and volatile build up (Cashman, 2004; Roman and Jaupart, 2014). Likewise, we infer that at the SE flank, an horizontal compressive stress generating by the crustal folding, prevents vertical propagation of dikes (Menand et al., 2010) and thus no scoria cones are emplaced.

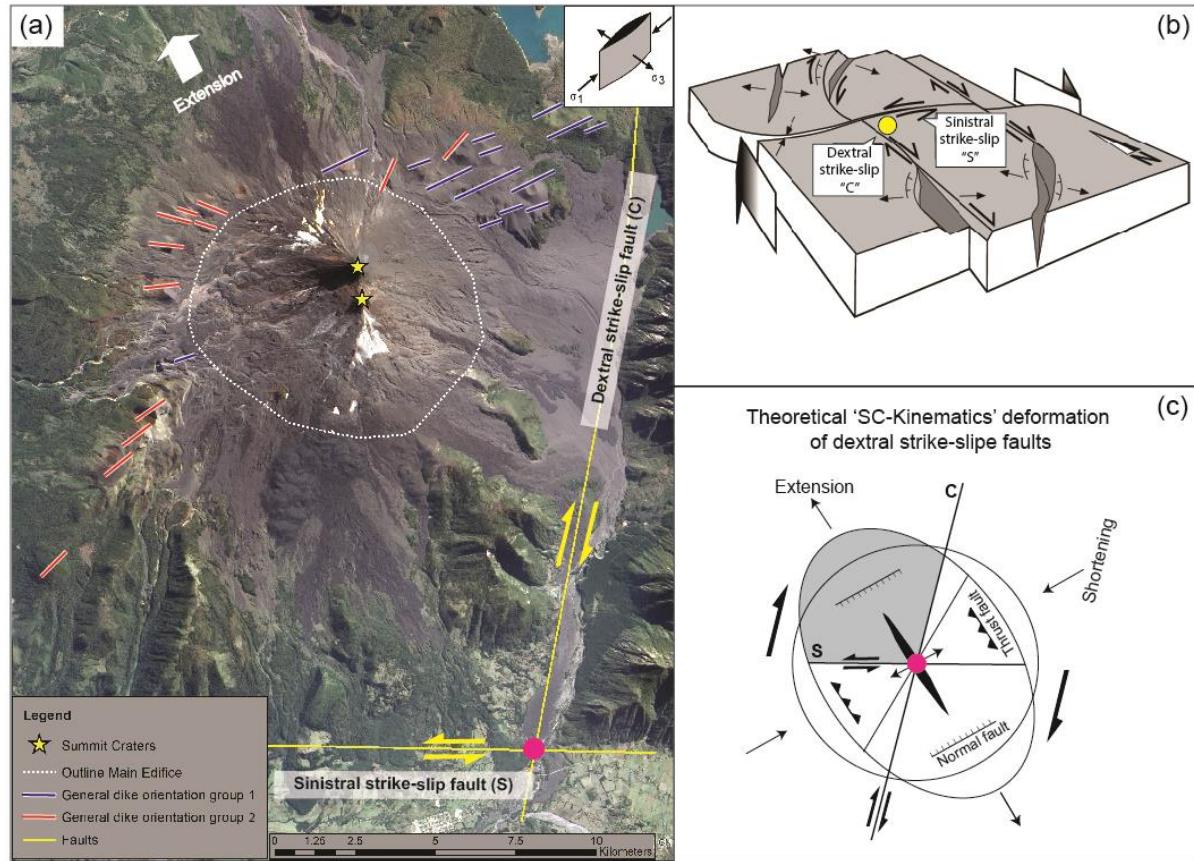


Figure 14. (a) Idealized diagram of dikes emplacement. Orientation of glomeroporphyritic dikes coincides with the regional σ_1 and pilotaxitic dikes propagate radial to the main edifice. Inset shows the orientation of the regional stress. (b) Model of crustal deformation at the northern end of the LOFZ according to Rosenau et al. (2006). Yellow dot shows our proposed spatial location of Llaima in the context of the model. (c) Theoretical ellipse of deformation for a SC-kinematics, modified from Rosenau et al. (2006). Gray area shows the location where we propose the Llaima system is located. Pink dot shows the location of the intersection between the Dextral strike-slip and Sinistral strike-slip faults, in both (a) and (c).

We assume that all dikes studied here, simply represent radial-to-the edifice trajectories, as evidences of cone-sheets and/or circumferential like intrusions were not recognized by us or had been reported elsewhere, to the best of our knowledge. Cone-sheets are associated to the overpressure of the reservoir and propagate in the σ_1 - σ_2 plane of the stress field caused by it

(Anderson, 1936; Mathieu et al., 2015). They occur above the shallow reservoir and are easily recognizable in eroded volcanic edifices (Burchardt et al., 2011). However, Llama is a persistently degassing volcano, which implies the constant reduction, by several MPa, of the reservoir pressure (Girona et al., 2014), thus decreasing the possibilities of cone-sheet emplacement. Ring-dike like intrusions are usually associated to the deviation of the stresses due to high mass removal, either by deglaciation, caldera formations and/or large lateral collapses (Corbi et al., 2015; Maccaferri et al., 2017). However, neither lateral collapses nor major deglaciation have occurred from the Holocene-to recent at Llama (Naranjo and Moreno, 1991). Thus, a considerable deviation of the stresses has not taken place and thus our proposed model for dike emplacement suitably describes the observed spatial distributions of the cones.

Further uncertainty arises due to the model of crustal deformation, as several different kinematic models (e.g. discontinues, continuous and quasi-continuous) have been proposed to explain to transcurrent deformation of strike-slip faults (Hernández-Moreno et al., 2014). At the LOFZ such models have been proposed by the study of rotation of crustal blocks of different sizes and shapes along the entire fault. However, paleo-magnetic results have demonstrated that the rotation pattern of blocks is not symmetrical along the LOFZ and thus any of the proposed models cannot account for the deformation along the entire fault zone (Hernández-Moreno et al., 2014). Therefore, the SC kinematics model proposed by Rosenau et al. (2006), which only considers the current deformation in the northern end of the LOFZ, can be considered adequate to explain the local-scale deformation in the area where Llama volcano is located.

Our results highlight the importance of the study of scoria cone compositional and textural variations in a local and regional tectonic context. We show how it is a powerful tool to assess and constrain complex volcanic plumbing, as significant petrological variations of scoria cone eruptions are linked to magmatic processes operating at depth and during dike emplacement. The latter controlled by the crustal stress and deformation. We believe that the approach presented here can be used in other systems associated with major tectonic features, where the study of petrologic characteristics of eruptive products can help in the understanding of how local tectonics interacts with the plumbing of volcanic systems.

6. Conclusions

The results of this work can then be summarized as follows:

- The petrological characteristics of the scoria cones at Llaima reflect two distinct groups that share a common source: the glomeroporphyritic and the pilotaxitic groups.
- Eruptive products from the glomeroporphyritic group are interpreted as result of magma recharge, followed by unimpeded dike intrusion and eruption. The propagation of the feeder dikes for this group is controlled by local extensional deformation of the crust, product of the regional tectonics.
- Eruptive products from the pilotaxitic group share a common origin with magmas from the glomeroporphyritic group, however compressional stress imposed by the load of the volcanic edifice, halts magma intrusion allowing mineral fractionation and volatile-pressure build up. The tensile stress exerted by the edifice controls the emplacement of the dikes, as they propagate in a radial pattern away from the volcano footprint. The single crystal populations recognize in this group are interpreted as a groundmass crystallization event during eruption, triggered by volatile decompression.

- The lack of scoria cones on the SE flank of Llaima, appears to be controlled by local-scale crustal deformation. This area coincides with an area folding and crustal horizontal compression, generated by the interaction between the synthetic Liquiñe-Ofqui fault, and its antithetic sinistral fault located south of the volcanic system.

Acknowledgments

We thank the University at Buffalo, and The Center for Geohazards Studies as their fully funded Schonwalder-Angel's PhD studies. We appreciate the constructive reviews of two anonymous reviewers and Professor Kelly Russell whose comments helped to clarify the manuscript. We also thank G. Valentine, A. Tibaldi, S. Pansino, D. Ruth-Sweeney, H. Murcia, F. Costa, C. Bouvet de Maisonneuve, and J. Maurice, for helpful discussions, also thanks to R. Leach, E. Breard for help during field seasons.

References

- Almeev, R.R., Kimura, J.I., Ariskin, A.A. and Ozerov, A.Y., 2013. Decoding crystal fractionation in calc-alkaline magmas from the Bezymianny Volcano (Kamchatka, Russia) using mineral and bulk rock compositions. *Journal of Volcanology and Geothermal Research*, 263(0): 141-171.
- Anderson, E.M., 1936. The Dynamics of the Formation of Cone-sheets, Ring-dykes, and Caldron-subsidences. *Proceedings of the Royal Society of Edinburgh* 56: 128–163.
- Biggar, G.M., 1966. Experimental studies of apatite crystallization in parts of the system CaO-P₂O₅-H₂O at 1000 bars. *Mineralogical Magazine and Journal of the Mineralogical Society*, 36(276): 1110-1122.
- Bouvet de Maisonneuve, C., Dungan, M.A., Bachmann, O. and Burgisser, A., 2012. Insights into shallow magma storage and crystallization at Volcán Llaima (Andean Southern Volcanic Zone, Chile). *Journal of Volcanology and Geothermal Research*, 211-212: 76-91.
- Bouvet De Maisonneuve, C., Dungan, M.A., Bachmann, O. and Burgisser, A., 2013. Petrological Insights into Shifts in Eruptive Styles at Volcán Llaima (Chile). *Journal of Petrology*, 54(2): 393-420.

- Browne, B.L., Eichelberger, J.C., Patino, L.C., Vogel, T.A., Dehn, J., Uto, K. and Hoshizumi, H., 2006. Generation of porphyritic and equigranular mafic enclaves during magma recharge events at Unzen volcano, Japan. *Journal of Petrology*, 47(2): 301-328.
- Burchardt, S., Tanner, D.C., Troll, V.R., Krumbholz, M. and Gustafsson, L.E., 2011. Three-dimensional geometry of concentric intrusive sheet swarms in the Geitafell and the Dyrfjöll volcanoes, eastern Iceland. *Geochemistry, Geophysics, Geosystems*, 12(7): n/a-n/a.
- Cashman, K. and Blundy, J., 2000. Degassing and crystallization of ascending andesite and dacite. *Philosophical Transactions of the Royal Society a-Mathematical Physical and Engineering Sciences*, 358(1770): 1487-1513.
- Cashman, K.V., 1993. Relationship between Plagioclase Crystallization and Cooling Rate in Basaltic Melts. *Contributions to Mineralogy and Petrology*, 113(1): 126-142.
- Cashman, K.V., 2004. Volatile controls on magma ascent and eruption. *State of the Planet: Frontiers and Challenges in Geophysics*, 150(150): 109-124.
- Cembrano, J., Herve, F. and Lavenu, A., 1996. The Liquine Ofqui fault zone: A long-lived intra-arc fault system in southern Chile. *Tectonophysics*, 259(1-3): 55-66.
- Cembrano, J. and Lara, L., 2009. The link between volcanism and tectonics in the southern volcanic zone of the Chilean Andes: A review. *Tectonophysics*, 471(1-2): 96-113.
- Corbi, F., Rivalta, E., Pinel, V., Maccaferri, F., Bagnardi, M. and Acocella, V., 2015. How caldera collapse shapes the shallow emplacement and transfer of magma in active volcanoes. *Earth and Planetary Science Letters*, 431: 287-293.
- Cortés, J., 2013. CFU-PINGU.
- Cortés, J., 2015. CFU, pp. <https://vhub.org/resources/cfu>.
- Cortés, J. and Palma, J., 2016. Petrological INput - Graphical oUtput.
- Cortés, J.A., 2009. On the Harker Variation Diagrams; A Comment on “The Statistical Analysis of Compositional Data. Where Are We and Where Should We Be Heading?” by Aitchison and Egozcue (2005). *Mathematical Geosciences*, 41(7): 817-828.
- Cortés, J.A., Wilson, M., Condliffe, E., Francalanci, L. and Chertkoff, D.G., 2005. The evolution of the magmatic system of Stromboli volcano during the Vancori period (26–13.8 ky). *Journal of Volcanology and Geothermal Research*, 147(1-2): 1-38.
- Deer, W., Howie, R. and Zussman, J., 1992. An introduction to the rock-forming minerals (second edition). Longman, Harlow, United Kingdom.
- Folguera, A., Ramos, V.A. and Melnick, D., 2002. Partición de la deformación en la zona del arco volcánico de los Andes neuquinos (36–39°S) en los últimos 30 millones de años. . *Revista Geológica de Chile* 29 (2): 151–165.
- Geshi, N., Kusumoto, S. and Gudmundsson, A., 2012. Effects of mechanical layering of host rocks on dike growth and arrest. *Journal of Volcanology and Geothermal Research*, 223: 74-82.

- Ghiorso, M.S. and Gualda, G.A.R., 2015. An H₂O–CO₂ mixed fluid saturation model compatible with rhyolite-MELTS. *Contributions to Mineralogy and Petrology*, 169(6): 53.
- Girona, T., Costa, F., Newhall, C. and Taisne, B., 2014. On depressurization of volcanic magma reservoirs by passive degassing. *Journal of Geophysical Research: Solid Earth*, 119(12): 8667-8687.
- Gladney, E. and Roelandts, I., 1988. 1987 Compilation of Elemental Concentration Data for USGS BHVO-1, MAG-1, QLO-1, RGM-1, SCo-1, SDC-1, SGR-1 and STM-1. *Geostandards Newsletter*, 12(2): 253-362.
- Green, T.H. and Watson, E.B., 1982. Crystallization of apatite in natural magmas under high pressure, hydrous conditions, with particular reference to 'Orogenic' rock series. *Contributions to Mineralogy and Petrology*, 79(1): 96-105.
- Gualda, G.A.R., Ghiorso, M.S., Lemons, R.V. and Carley, T.L., 2012. Rhyolite-MELTS: a Modified Calibration of MELTS Optimized for Silica-rich, Fluid-bearing Magmatic Systems. *Journal of Petrology*, 53(5): 875-890.
- Gudmundsson, A., 2006. How local stresses control magma-chamber ruptures, dyke injections, and eruptions in composite volcanoes. *Earth-Science Reviews*, 79(1-2): 1-31.
- Gudmundsson, A., 2012. Magma chambers: Formation, local stresses, excess pressures, and compartments. *Journal of Volcanology and Geothermal Research*, 237(0): 19-41.
- Hammer, J.E. and Rutherford, M.J., 2002. An experimental study of the kinetics of decompression-induced crystallization in silicic melt. *Journal of Geophysical Research-Solid Earth*, 107(B1): ECV 8-1-ECV 8-24.
- Hernández-Moreno, C., Speranza, F. and Di Chiara, A., 2014. Understanding kinematics of intra-arc transcurrent deformation: Paleomagnetic evidence from the Lique-Ofqui fault zone (Chile, 38-41 degrees S). *Tectonics*, 33(10): 1964-1988.
- Hickey-Vargas, R., Holbik, S., Tormey, D., Frey, F.A. and Roa, H.M., 2016. Basaltic rocks from the Andean Southern Volcanic Zone: Insights from the comparison of along-strike and small-scale geochemical variations and their sources. *Lithos*, 258: 115-132.
- Higgins, M., 2006. Quantitative textural measurements in igneous and metamorphic petrology. Cambridge University Press, New York, United States of America, 265 pp.
- Irvine, T. and Baragar, W., 1971. A Guide to the Chemical Classification of the Common Volcanic Rocks. *Canadian Journal of Earth Sciences*, 8(5): 523-548.
- Jeffery, A.J., Gertisser, R., Troll, V.R., Jolis, E.M., Dahren, B., Harris, C., Tindle, A.G., Preece, K., O'Driscoll, B., Humaida, H. and Chadwick, J.P., 2013. The pre-eruptive magma plumbing system of the 2007-2008 dome-forming eruption of Kelut volcano, East Java, Indonesia. *Contributions to Mineralogy and Petrology*, 166(1): 275-308.
- Johnson, E.R., Wallace, P.J., Cashman, K.V., Granados, H.D. and Kent, A.J.R., 2008. Magmatic volatile contents and degassing-induced crystallization at Volcan Jorullo, Mexico: Implications for melt evolution and the plumbing systems of monogenetic volcanoes. *Earth and Planetary Science Letters*, 269(3-4): 477-486.

- Lara, L.E., Cembrano, J. and Lavenu, A., 2008. Quaternary Vertical Displacement along the Liquiñe-Ofqui Fault Zone: Differential Uplift and Coeval Volcanism in the Southern Andes? *International Geology Review*, 50(11): 975-993.
- LeMaitre, R., Streckcisen, A., Zanettin, B., Le Bas, M., Bonin, B., Bateman, P., Bellieni, G., Dudek, A., Efremova, J., Keller, J., Lameyre, J., Sabine, P., Schmidt, R., Sorensen, H. and Wooley, A., 2002. Igneous rocks. A classification and glossary of terms. Recommendations of the International Union of Geological Sciences Subcommission on the systematics of igneous rocks, University Press, Cambridge.
- Maccaferri, F., Richter, N. and Walter, T.R., 2017. The effect of giant lateral collapses on magma pathways and the location of volcanism. *Nat Commun*, 8(1): 1097.
- Marsh, B., 1988. Crystal size distribution (CSD) in rocks and the kinetics and dynamics of crystallization. I. Theory. *Contributions to Mineralogy and Petrology*, 99: 277-291.
- Mathieu, L., Burchardt, S., Troll, V.R., Krumbholz, M. and Delcamp, A., 2015. Geological constraints on the dynamic emplacement of cone-sheets - The Ardnamurchan cone-sheet swarm, NW Scotland. *Journal of Structural Geology*, 80: 133-141.
- Melnick, D., Rosenau, M., Folguera, A. and Echtler, H., 2006. Neogene tectonic evolution of the Neuquén Andes western flank (37–39°S). *Geological Society of America Special Papers*, 407: 73-95.
- Menand, T., Daniels, K.A. and Benghiat, P., 2010. Dyke propagation and sill formation in a compressive tectonic environment. *Journal of Geophysical Research-Solid Earth*, 115(B8): B08201.
- Mollo, S. and Hammer, J.E., 2017. Dynamic crystallization in magmas, Mineral reaction kinetics: Microstructures, textures, chemical and isotopic signatures, pp. 378-418.
- Mollo, S., Lanzafame, G., Masotta, M., Iezzi, G., Ferlito, C. and Scarlato, P., 2011. Cooling history of a dike as revealed by mineral chemistry: A case study from Mt. Etna volcano. *Chemical Geology*, 288(1-2): 39-52.
- Morimoto, N., 1989. Nomenclature of Pyroxenes. *Canadian Mineralogist*, 27(1): 143-156.
- Muller, J.R., Ito, G. and Martel, S.J., 2001. Effects of volcano loading on dike propagation in an elastic half-space. *Journal of Geophysical Research-Solid Earth*, 106(B6): 11101-11113.
- Nakamura, K., 1977. Volcanos as Possible Indicators of Tectonic Stress Orientation - Principle and Proposal. *Journal of Volcanology and Geothermal Research*, 2(1): 1-16.
- Naranjo, J. and Moreno, H., 1991. Actividad explosiva postglacial en el Volcán Llaima, Andes del Sur (38 S). *Revista Geológica de Chile*, 18(1): 69-80.
- Naranjo, J. and Moreno, H., 2005. Geología del Volcán Llaima, Región de la Araucanía. Servicio Nacional de Geología y Minería, Carta Geológica de Chile, Santiago, Chile.
- Nicholls, J., 1988. The Statistics of Pearce Element Diagrams and the Chayes Closure Problem. *Contributions to Mineralogy and Petrology*, 99(1): 11-24.

- Nicholls, J. and Russell, K., 1990. Pearce element ratios -An overview, example and bibliography. In: K. Russell and C. Stanley (Editors), Geological Association of Canada, Short Courses Notes 8, Vancouver, pp. 11-21.
- Pardo-Casas, F. and Molnar, P., 1987. Relative motion of the Nazca (Farallon) and South American Plates since Late Cretaceous time. *Tectonics*, 6(3): 233-248.
- Pearce, H., 1968. A Contribution to the theory of variation diagrams. *Contributions to Mineralogy and Petrology*, 19: 142-157.
- Petit-Breuilh, M., 2006. La Historia Eruptiva de los volcanes Hispanoamericanos (Siglos XVI al XX). Servicio de Publicaciones Exmo., Huelva, Spain.
- Pinel, V. and Jaupart, C., 2000. The effect of edifice load on magma ascent beneath a volcano. *Philosophical Transactions of the Royal Society of London. Series A: Mathematical, Physical and Engineering Sciences*, 358(1770): 1515-1532.
- Poland, M.P., Fink, J.H. and Tauxe, L., 2004. Patterns of magma flow in segmented silicic dikes at Summer Coon volcano, Colorado: AMS and thin section analysis. *Earth and Planetary Science Letters*, 219(1): 155-169.
- Rollinson, H., 1993. Using geochemical data: Evaluation, presentation, interpretation. Longman, Scientific and Technical.
- Roman, A. and Jaupart, C., 2014. The impact of a volcanic edifice on intrusive and eruptive activity. *Earth and Planetary Science Letters*, 408: 1-8.
- Rosenau, M., Melnick, D. and Echtler, H., 2006. Kinematic constraints on intra-arc shear and strain partitioning in the southern Andes between 38 degrees S and 42 degrees S latitude. *Tectonics*, 25(4): TC4013.
- Ruth, D.C.S., 2014. Physical and geochemical systematics of the 2008 violent Strombolian eruption of Llaima volcano, Chile, University at Buffalo, The State University of New York, Buffalo, NY, USA.
- Ruth, D.C.S., Cottrell, E., Cortes, J.A., Kelley, K.A. and Calder, E.S., 2016. From Passive Degassing to Violent Strombolian Eruption: the Case of the 2008 Eruption of Llaima Volcano, Chile. *Journal of Petrology*, 57(9): 1833-1864.
- Rutherford, M.J., 2008. Magma Ascent Rates. *Minerals, Inclusions and Volcanic Processes*, 69(1): 241-271.
- Schmidt, M.E. and Gruner, A.L., 2011. Deep Mafic Roots to Arc Volcanoes: Mafic Recharge and Differentiation of Basaltic Andesite at North Sister Volcano, Oregon Cascades. *Journal of Petrology*, 52(3): 603-641.
- Schonwalder-Angel, D., 2015. The Emplacement of Satellite Scoria Cones at LLaima Volcanic System, Chile; The Interaction Between Magmatic Overpressure and the Local Tectonics, University at Buffalo, the State University of New York, Buffalo, NY, USA, 262 pp.

- Sparks, R.S.J. and Cashman, K.V., 2017. Dynamic Magma Systems: Implications for Forecasting Volcanic Activity. *Elements*, 13(1): 35-40.
- Stern, C., Moreno, H., Lopez-Escobar, L., Clavero, J., Lara, L.E., Naranjo, J.A. and Parada, M.A., 2007. Chilean Volcanoes. In: T. Moreno and W. Gibbons (Editors), *The Geology of Chile*. The Geological Society, London, pp. 147-178.
- Streck, M.J., 2008. Mineral Textures and Zoning as Evidence for Open System Processes. *Minerals, Inclusions and Volcanic Processes*, 69(1): 595-622.
- Strong, M. and Wolff, J., 2003. Compositional variations within scoria cones. *Geology*, 31(2): 143-146.
- Sun, S. and McDonough, W.F., 1989. Chemical and isotopic systematics of oceanic basalts: implications for mantle composition and processes. Geological Society, London, Special Publications, 42(1): 313-345.
- Szramek, L., Gardner, J.E. and Larsen, J., 2006. Degassing and microlite crystallization of basaltic andesite magma erupting at Arenal volcano, Costa Rica. *Journal of Volcanology and Geothermal Research*, 157(1-3): 182-201.
- Takada, A., 1994. The Influence of Regional Stress and Magmatic Input on Styles of Monogenetic and Polygenetic Volcanism. *Journal of Geophysical Research-Solid Earth*, 99(B7): 13563-13573.
- Terashima, S., Taniguchi, M., Mikoshiba, M. and Imai, N., 1998. Preparation of two new GSJ geochemical reference materials: Basalt JB-1b and coal fly ash JCFA-1. *Geostandards Newsletter-the Journal of Geostandards and Geoanalysis*, 22(1): 113-117.
- Tibaldi, A., 1995. Morphology of pyroclastic cones and tectonics. *Journal of Geophysical Research-Solid Earth*, 100(B12): 24521-24535.
- Tibaldi, A., 2015. Structure of volcano plumbing systems: A review of multi-parametric effects. *Journal of Volcanology and Geothermal Research*, 298: 85-135.
- Toplis, M.J. and Carroll, M.R., 1995. An Experimental Study of the Influence of Oxygen Fugacity on Fe-Ti Oxide Stability, Phase Relations, and Mineral—Melt Equilibria in Ferro-Basaltic Systems. *Journal of Petrology*, 36(5): 1137-1170.
- Tormey, D., Hickey-Vargas, R., Frey, F. and Lopez-Escobar, L., 1991. Recent lavas from the Andean volcanic front (33 to 42 S); Interpretations of along-arc compositional variations. *Geological Society of America Special Papers*, 265: 57-77.
- Valentine, G.A. and Krogh, K.E.C., 2006. Emplacement of shallow dikes and sills beneath a small basaltic volcanic center - The role of pre-existing structure (Paiute Ridge, southern Nevada, USA). *Earth and Planetary Science Letters*, 246(3-4): 217-230.
- van Wyk de Vries, B. and Merle, O., 1998. Extension induced by volcanic loading in regional strike-slip zones. *Geology*, 26(11): 983.
- Wilson, M., 1989. *Igneous Petrogenesis*. Springer, Dordrecht, The Netherlands, 466 pp.

ACCEPTED MANUSCRIPT

Highlights

- The scoria cones at Llaima volcano, represent two distinct groups, based in their composition, textures and mineral chemistry.
- The groups represent the interplay of processes occurring at the magma reservoir and during dike emplacement.
- Dike emplacement at Llaima is linked to the state of the stress at the crust and its response to the volcanic system and the influence of the Liquiñe-Ofqui Fault Zone.